Geodetic Strain Rates for the 2022 Update of the New Zealand National Seismic Hazard Model

Jeremy Maurer*¹, Kaj Johnson², Laura M. Wallace^{3,4,5}, Ian Hamling⁶, Charles A. Williams⁶, Chris Rollins³, Matt Gerstenberger⁶, and Russ Van Dissen⁶

ABSTRACT

Geodetic data in plate boundary zones reflect the accrual of tectonic strain and stress, which will ultimately be released in earthquakes, and so they can provide valuable insights into future seismic hazards. To incorporate geodetic measurements of contemporary deformation into the 2022 revision of the New Zealand National Seismic Hazard Model 2022 (NZ NSHM 2022), we derive a range of strain-rate models from published interseismic Global Navigation Satellite Systems velocities for New Zealand. We calculate the uncertainty in strain rate excluding strain from the Taupō rift-Havre trough and Hikurangi subduction zone, which are handled separately, and the corresponding moment rates. A high shear strain rate occurs along the Alpine fault and the North Island dextral fault belt, as well as the eastern coast of the North Island. Dilatation rates are primarily contractional in the South Island and less well constrained in the North Island. Total moment accumulation derived using Kostrov-type summation varies from 0.64 to 2.93 x 10¹⁹ N·m/yr depending on method and parameter choices. To account for both aleatory and epistemic uncertainty in the strain-rate results, we use four different methods for estimating strain rate and calculate various average models and uncertainty metrics. The maximum shear strain rate is similar across all methods, whereas the dilatation rate and overall strain rate style differ more significantly. Each method provides an estimate of its own uncertainty propagated from the data uncertainties, and variability between methods provides an additional estimate of epistemic uncertainty. Epistemic uncertainty in New Zealand tends to be higher than the aleatory uncertainty estimates provided by any single method, and epistemic uncertainty on dilatation rate exceeds the aleatory uncertainty nearly everywhere. These strain-rate models were provided to the NZ NSHM 2022 team and used to develop fault-slip deficit rate models and scaled seismicity rate models.

KEY POINTS

- We derive strain rates for New Zealand from published interseismic Global Navigation Satellite Systems velocities using four methods.
- Strain rates are similar across methods, but differences are larger than single-model uncertainty.
- Strain rates are broadly consistent with geologic faulting style and estimated moment accumulation rates.

Supplemental Material

INTRODUCTION

Since the early 1990s, our understanding of plate boundary zone crustal deformation has been revolutionized by advances in satellite-based geodetic techniques, especially Global Navigation Satellite Systems (GNSS), which enable precise tracking of ground movement and measurement of crustal deformation within plate boundary zones. These measurements have

constrained the distribution and rate of tectonic strain accumulation in regions around the world (e.g., Kreemer *et al.*, 2000; Beavan and Haines, 2001a; Shen *et al.*, 2015; Haines and Wallace, 2020). Geodetic data can provide information on active fault-slip rates and potential seismic hazards independently of geological and paleoseismological estimates. For example, the

Cite this article as Maurer, J., K. Johnson, L. M. Wallace, I. Hamling, C. A. Williams, C. Rollins, M. Gerstenberger, and R. Van Dissen (2023). Geodetic Strain Rates for the 2022 Update of the New Zealand National Seismic Hazard Model, *Bull. Seismol. Soc. Am.* **114**, 57–77, doi: 10.1785/0120230145

© Seismological Society of America

^{1.} Department of Geosciences and Geological and Petroleum Engineering, University of Missouri Science and Technology, Rolla, Missouri, U.S.A., (a) https://orcid.org/0000-0002-3624-5961 (JM); 2. Department of Earth and Atmospheric Sciences, Indiana University, Bloomington, Indiana, U.S.A., (b) https://orcid.org/0000-0003-1511-5241 (KJ); 6. GNS Science, Lower Hutt, New Zealand, (b) https://orcid.org/0000-0003-4324-274X (IH); (b) https://orcid.org/0000-0001-7435-9196 (CAW); (c) https://orcid.org/0000-0002-0392-7114 (MG); (c) https://orcid.org/0000-0001-8224-7573 (RVD); 3. University of Texas Institute for Geophysics, Austin, Texas, U.S.A., (b) https://orcid.org/0000-0002-5291-6956 (CR); 4. GEOMAR Helmholtz Centre for Ocean Research Kiel, Kiel, Germany; 5. Institute of Geosciences, Christian-Albrechts-Universität zu Kiel, Kiel, Germany

^{*}Corresponding author: jmaurer@mst.edu

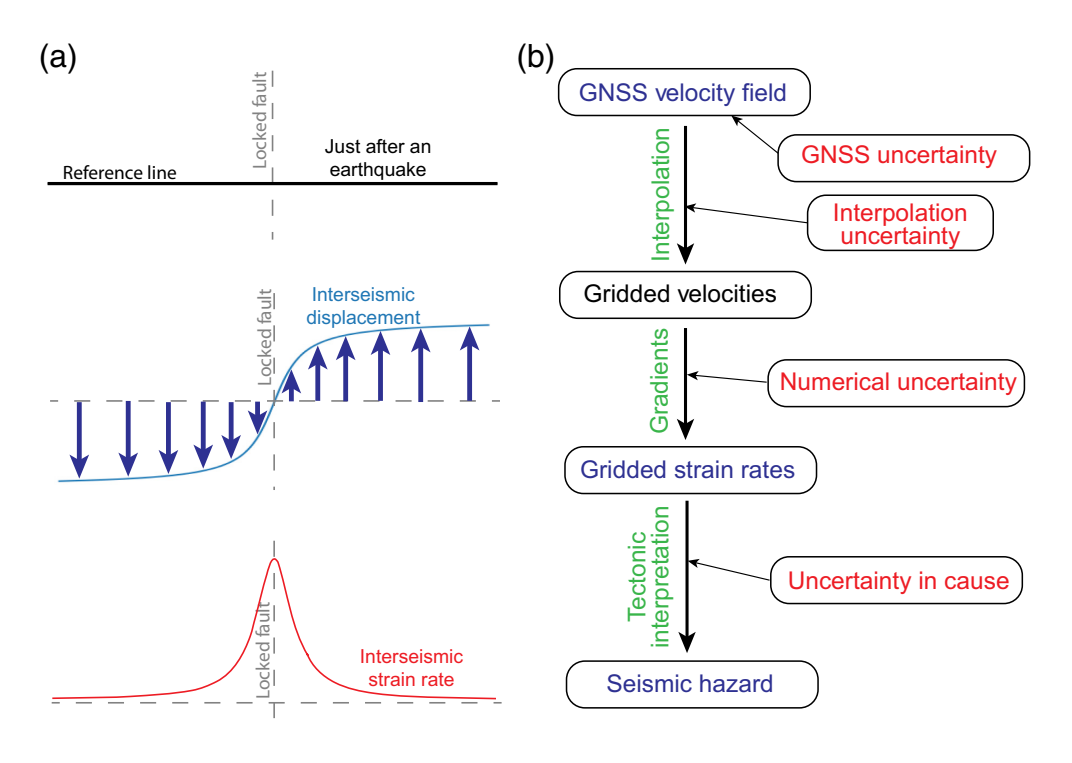


Figure 1. (a) Cartoon diagram illustrating the displacement signal crossing a fault as might be measured by Global Navigation Satellite Systems (GNSS) and the resulting strain-rate profile. (b) Sources of uncertainty in estimating and interpreting geodetic strain rates. Bold represents larger contributions to the overall uncertainty. The color version of this figure is available only in the electronic edition.

2014 and 2023 versions of the U.S. National Seismic Hazard Model (US NSHM; Petersen et al., 2014; Pollitz et al., 2022) and version 3 of the Unified California Earthquake Rupture Forecast (UCERF3; Field et al., 2014) used geodetically derived deformation models (fault-slip rates) among the logic-tree branches. However, slip and slip accumulation on known faults does not capture all of the deformation in plate boundary regions. In the geodetic deformation models in UCERF3 (Field et al., 2014), 20%-30% of the total deformation is attributed to distributed off-fault deformation (Field et al., 2014), and in the geodetic deformation models in the US NSHM, 30%-60% of the total model moment rate is attributed to off-fault strain rate (Pollitz et al., 2022). The off-fault deformation in US NSHM 2014 and UCERF3 geodetic deformation models was not used directly in hazard calculations, due in part to uncertainty regarding how present-day (i.e., instantaneous) strain rates relate to seismic hazard assessment and in part to a lack of confidence in the robustness of model estimates. To be useful, strain rates derived from GNSS need to have associated uncertainties and be interpreted in terms of seismic moment accumulation rate, either through direct volume-based calculation (Kostrov, 1974; Savage and Simpson, 1997; Stevens and Avouac, 2021) or by calculating fault-slip rates (Johnson et al., 2022). Geodetic strain rate has also recently begun to be used directly in seismic hazard models. Bird et al. (2015), Rhoades et al. (2017), and Rastin et al. (2022, 2023) combined geodetically derived strain rates with smoothed seismicity rates to obtain joint smooth seismicity predictions. Beyond this, in some recent studies, strain rate has been shown to correlate to the background seismicity rate (Zeng *et al.*, 2018; Stevens and Avouac, 2021) and the rate of major earthquakes (Hussain *et al.*, 2018).

Most tectonic strain measured by GNSS is assumed to be elastic, accumulating in the Earth's crust during the "interseismic" time between earthquakes (Savage, 1983; Mazzotti et al., 2000; McCaffrey et al., 2000; Wallace et al., 2004). In the classic elastic earthquake cycle model (Reid, 1910), interseismic strain arises when two pieces of crust are prevented from sliding past one another along a fault by the friction on the fault interface. If the

present-day rate of strain accumulation is representative of the long-term average, the measured interseismic strain rate can be used to estimate how much strain has accumulated since the last earthquake (Fig. 1a).

Although simple in concept, there are many complications to estimating strain rate in practice because the largest interseismic strain rates, even around major fault systems, are usually <0.5 microstrain (0.5×10^{-6} strain) per year, or 0.5 mm change over a kilometer. Accurately measuring such small deformation signals requires accounting for several sources of error. Figure 1b summarizes the steps to calculate strain rates and the associated uncertainties with each step. GNSS velocity estimation requires correction of any nontectonic and transient deformation, for example, during and following a large earthquake when large displacements of the ground can occur. These signals produce large, measurable strains that can far exceed those from interseismic strain accumulation, so they must be removed. Nontectonic signals, such as uplift and subsidence due to hydrological processes, can contaminate the tectonic strain signal. There is uncertainty in the velocity estimation procedure related to the number and quality of measurements made. All of these issues mean that the GNSS velocities used to determine strain rates have associated uncertainties. Strain rates from GNSS are computed from irregularly spaced data, often requiring interpolation to obtain gridded velocities for numerical differentiation,

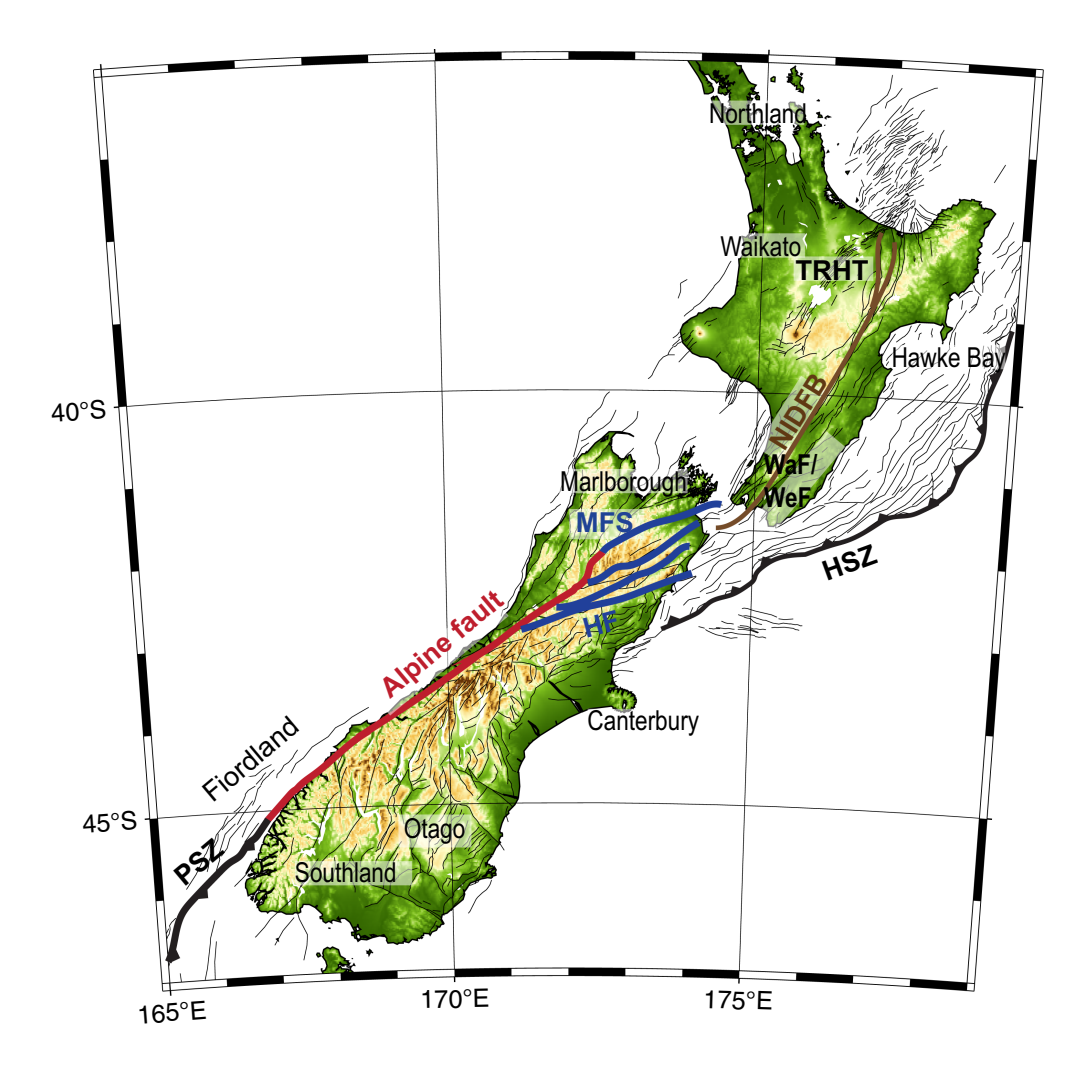


Figure 2. Tectonic setting in New Zealand showing major fault systems and areas referenced in the main text. Thin lines show active fault traces from the NZ Community Fault Model v.1.0 (Seebeck *et al.*, 2022, 2023). HF, Hope fault; HSZ, Hikurangi subduction zone; MFS, Marlborough fault system; NIDFB, North Island dextral fault belt; PSZ, Puysegur subduction zone; TRHT, Taupō rift—Havre trough; WaF/WeF, Wairarapa fault and Wellington fault. The color version of this figure is available only in the electronic edition.

which introduces another potential source for error. There is some uncertainty in the numerical differentiation procedure, but practically speaking, it is much lower than other sources given appropriate grid spacing. Hearn et al. (2010) and Sandwell et al. (2016) compared a suite of 17 strain rate methods in southern California and found that variability between methods was up to 100% of the signal in some places; however, in that case, the data sets used in each method were different. A follow-up analysis of the same 17 models by Xu et al. (2021) showed that, on average, all models were highly correlated at long wavelengths (>100 km) and approached a correlation of zero at length scales of roughly 30 km and below. These studies compared both model- and data-based methods for calculating strain rates; however, model-based strain rates are usually limited to explaining strain accumulating on faults, and the presence of significant off-fault strain (e.g., Johnson, 2013) could result in a bias between model- and

data-based methods. Finally, there is the issue of interpreting the estimated strain rates themselves. The determination of how much of a given strain field is associated with future earthquake potential and where that potential is located (i.e., which faults are accumulating strain) is the final source of uncertainty and a critical step for incorporating strain rates into seismic hazard assessment.

To incorporate geodetic measurements of contempodeformation into the 2022 revision of the New Zealand National Seismic Hazard Model (NZ NSHM 2022; Johnson et al., 2022; K. Johnson et al., unpublished manuscript, see Data and Resources), we develop a range of strain rate models using New Zealand's interseismic campaign Global Positioning System (GPS)-derived velocity spanning 1995–2013 (Beavan et al., 2016). These models were used to solve for slip deficit rates on the same faults being used in the NZ NSHM 2022 fault model (Johnson et al., 2022). We use several different methods

for computing strain rates to quantify epistemic uncertainty in the strain rates. We show how different assumptions made by different strain rate methods influence the resulting strain rate field and discuss how to handle multiple strain rate methods within a seismic hazard scenario. We also discuss the implications of the results drawn from the suite of strain rate models for seismic hazards in New Zealand (Fig. 2).

DATA

This project makes use of the comprehensive GNSS campaign velocity field for New Zealand collected under the leadership of the late John Beavan (Beavan et al., 2016; Fig. 3). The velocity field is based on data acquired between 1995 and 2013 and includes corrections for recent earthquakes during that period, such as the 2010/2011 Canterbury earthquake sequence, to best represent interseismic rather than coseismic and postseismic deformation. The campaign GNSS network

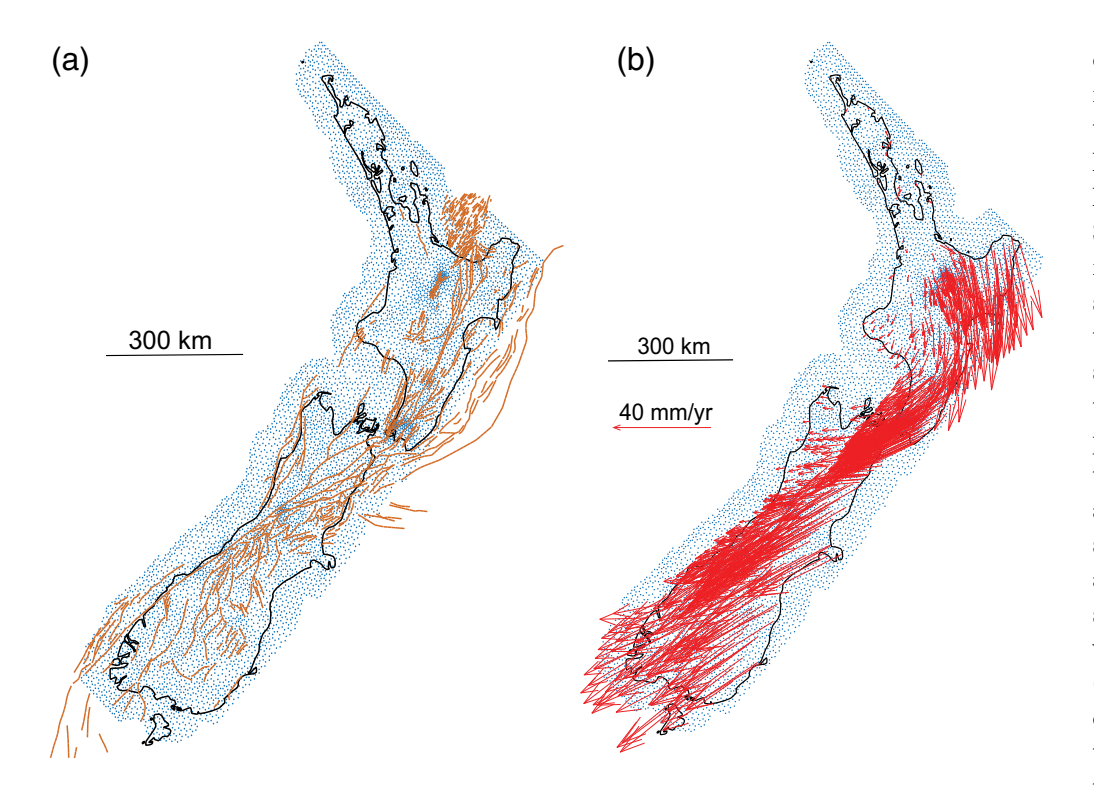


Figure 3. Grid constructed for the strain-rate interpolation, with (a) faults shown on the grid and (b) GNSS velocities (red arrows) in a fixed Australian plate reference. The GNSS field shown is the corrected one discussed in the Data section, with modeled velocities due to subduction zone locking and TRHT contraction removed. The mesh size is determined by the density of Global Positioning System-velocity observation coordinates. Each of the four methods provides velocity and strain rate interpolated to the same set of grid nodes for direct comparison. The color version of this figure is available only in the electronic edition.

is relatively dense, with average site spacing between sites of <10–20 km, varying from around 5 km in more densely sampled areas to 50 km in less tectonically active regions (such as the Northland and Waikato regions). We use this velocity field to estimate the surface strain rate using the various methods discussed in the Methods section. Formal uncertainties exist for the GNSS velocity field (Fig. S1, available in the supplemental material to this article) but are nearly all <3 mm/yr, and not all strain-rate methods make use of them. We discuss uncertainties in the derived strain-rate fields and the influence of data uncertainty in the Discussion section.

Velocities from continuous GNSS stations are available in New Zealand but were not included in the analyzed velocity field. This was because the available continuous stations have several issues that would require careful analysis to resolve, which was beyond the scope of the NZ NSHM project. These issues include (1) the presence of transient displacements, including coseismic and postseismic displacements from several large earthquakes in the past decade, and slowslip events (SSEs) for stations on the North Island; (2) the available continuous data on the North Island spans a different time period and SSE cycle than the campaign stations. This

could result in strain that is related to uneven sampling of the SSE cycle and does not have to do with interseismic locking on crustal faults; (3) South Island stations are primarily clustered in several small regions, so the contribution to constraining the overall strain rate is small; (4) the fact that the continuous and campaign stations have different time periods of coverage would also require careful comparison to ensure consistency; and (5) finally, the continuous stations are sparser than the very dense campaign network (937 campaign vs. 238 continuous stations). As a result of these considerations and the time limitations of publishing the 2022 NSHM, we restricted ourselves to using the peerreviewed and published GNSS velocity field of Beavan et al. (2016). We recommend that future studies undertake a full analysis of the continuous and campaign station networks

to incorporate these into a unified velocity field in New Zealand.

Before calculating strain rates, we removed contributions to the velocity field from contraction in the Taupō rift-Havre trough (TRHT) region. Strain from the TRHT is due to cooling of the magma body and is not related to elastic coupling on faults, so we exclude it from our strain-rate calculations. For the contraction and subsidence throughout the central TRHT, we use an updated model of Hamling et al. (2015), which includes additional synthetic aperture radar data up to 2020. The model consists of a horizontal set of tensile dislocations to represent the cooling and contraction of a sill-like body at 9.5 km depth. The model is discretized into ~1900 individual patches, and we solve for the best-fitting contraction at each patch. We follow the method of Hamling, Kilgour, et al. (2022) and use regional magnetotelluric data to help constrain the spatial extent of contraction. The best-fitting model, which predicts a volume loss of ~0.02 km³/yr, is used to remove the expected horizontal contraction rates from the interseismic velocity field.

In addition to the strain signals in the TRHT, we also model and remove strain due to coupling on the Hikurangi subduction zone (HSZ). This is because the HSZ is modeled separately in the NZ NSHM 2022. We take advantage of

well-established block modeling methods to invert the velocity field for Hikurangi subduction interface coupling (Wallace *et al.*, 2004, 2012) and subtract the component of deformation due to elastic strain from Hikurangi locking from the Beavan *et al.* (2016) velocity field. We use the remaining field (also corrected for the TRHT signal described earlier) to derive the strain-rate maps.

METHODS

It is not possible to estimate the complete strain tensor field without knowledge of the full (i.e., spatially continuous) 3D velocity field and variations with depth, and for tectonic applications, the length scale required to accurately sample deformation is typically on the order of a few kilometers. Geodetic data such as GNSS provide spatially scattered data on the surface of the Earth, usually at a spacing much greater than a few kilometers. Therefore, in seismic hazard applications, horizontal components of the surface strain rate field are computed through interpolation, and it is often assumed that the 2D strain field is representative of strain at depth. Numerous methods and algorithms have been proposed for this purpose, but few published studies have systematically explored the differences between strain rate methods or the implications of the different methodologies for understanding crustal strain rates. Wu et al. (2011) discuss a few different methods and suggest that using spatial covariance information improves the fit and reduces artifacts in the interpolated strain-rate field. Baxter et al. (2011) discuss problems with calculating strain rates from sparse velocity observations and show that artifacts can be present. Hearn et al. (2010) and Sandwell et al. (2016) compared a suite of 17 strain rate methods in southern California and found that variability between methods was nearly 100% of the signal in some places. Maurer and Materna (2023) applied four different strain rate methods to the same data set and study area to calculate the epistemic uncertainty arising from the choice of strain rate model. They found that the variability between methods differs from the uncertainty estimates of a given method and that it is important to consider both the aleatory and epistemic uncertainties when using strain rates for seismic hazard analysis. Given the diversity of approaches developed to determining strain rates from GNSS velocity fields and the need to quantify both epistemic and aleatory uncertainty in the strain rates, we use four different methods to compute four strain rate maps for New Zealand. Ultimately, the suite of strain rate models has been incorporated into geodetic slip rate deficit estimates for the NZ NSHM 2022 (Johnson et al., 2022; K. Johnson et al., unpublished manuscript, see Data and Resources).

Surface strain rate and seismic hazard

The horizontal surface strain rate tensor is a symmetric, positive-definite tensor with three independent components represented by

$$\dot{\varepsilon}_{ij} = \frac{1}{2} \left(\frac{dv_i}{dx_i} + \frac{dv_j}{dx_i} \right),\tag{1}$$

in which v_i is the *i*th component of the velocity of the surface. Here, we focus on surface strain rates, so i, j = 1,2. The "principal strain rates" are defined as the eigenvalues of the strain rate tensor: $\dot{\varepsilon}_1$ and $\dot{\varepsilon}_2$. Two invariants are of particular importance: one-half the trace of the strain rate tensor, which equals the areal strain rate or dilatation (change in area):

$$\dot{\Delta}A = 0.5(\dot{\varepsilon}_{11} + \dot{\varepsilon}_{22}) = 0.5(\dot{\varepsilon}_1 + \dot{\varepsilon}_2),\tag{2}$$

and the maximum (engineering) shear strain rate,

$$\dot{\gamma} = \sqrt{(\dot{\varepsilon}_{11} - \dot{\varepsilon}_{22})^2 + 4\dot{\varepsilon}_{12}^2} = \dot{\varepsilon}_1 - \dot{\varepsilon}_2. \tag{3}$$

Under this convention, the dilatation rate is positive for extension and negative for contraction. Savage and Simpson (1997) considered the relation between strain and seismic moment accumulation rates (see Text S1). The interseismic moment deficit rate (MDR) for a given fault can be defined as

$$\dot{M}_d = G\dot{s}A_f,\tag{4}$$

for shear modulus G, mean slip deficit rate \dot{s} , and the seismogenic fault area A_f . Savage and Simpson (1997) suggest that the minimum MDR can be calculated from the surface strain rate by assuming a seismogenic volume (surface area times seismogenic thickness, H) and the maximum principal strain rates $|\dot{\varepsilon}^{\max}| = \max\{|\dot{\varepsilon}_1|,|\dot{\varepsilon}_2|,|\dot{\varepsilon}_1+\dot{\varepsilon}_2|\}$:

$$\dot{M}_d \ge 2GH \int_{A_s} |\dot{\varepsilon}^{\max}| dA,$$
 (5)

in which A_s is the total surface area under consideration. The assumption here is that the estimated surface strain rate is constant with depth.

We can also calculate the style of faulting that would be expected based only on strain rate; in general, this need not be the actual faulting style because earthquake faulting corresponds to total stress, not to incremental strain rate. With this caveat, we can use

$$s = \frac{\dot{\varepsilon}_1 + \dot{\varepsilon}_2}{|\dot{\varepsilon}_1| + |\dot{\varepsilon}_2|},\tag{6}$$

in which s ranges from -1 to +1 to represent the faulting style implied by the instantaneous strain rate, with -1 representing normal faulting, 0 representing strike-slip faulting, and +1 representing thrust faulting.

Methods for generating strain rate maps

For 2D surfaces, determining the strain rate at every point in space requires some form of interpolation scheme. Methods for calculating strain rate can be broken into several broad classes, including direct calculation from baselines (e.g., Cai and Grafarend, 2007), fitting the velocity field using various basis functions (e.g., Feigl et al., 1993; Haines and Holt, 1993; Beavan and Haines, 2001b; Hackl et al., 2009; Tape et al., 2009; Wang and Wright, 2012; Kreemer et al., 2014; Weiss et al., 2020), and using basis functions from elasticity theory (e.g., Noda and Matsu'ura, 2010; Haines et al., 2015; Sandwell and Wessel, 2016). Other common approaches include using spatial weighting functions with least squares (e.g., kriging) (e.g., Shen et al., 1996; Kato et al., 1998; El-Fiky and Kato, 1999; Goudarzi et al., 2015; Shen et al., 2015; Tarayoun et al., 2018; Maurer and Materna, 2023) or moving windows (e.g., Handwerger et al., 2019; Huang et al., 2022). When calculating strain rates using baselines, errors get directly propagated to the solution, so baseline strain rate estimates tend to be noisy. Basis function methods typically involve velocity interpolation to a spatially regular grid and the numerical calculation of derivatives to compute strain rates. The other methods may use interpolation or may directly solve for strain rates on any specified (potentially unstructured) grid. Numerical derivatives, for sufficiently dense node spacing, are not a large source of error compared with the interpolation step itself, whereas the interpolation process can involve large uncertainties when interpolating sparse geodetic velocities. Methods from the aforementioned different classes clearly involve different types of assumptions about the underlying velocity field, and thus the interpolation method chosen is a source of epistemic uncertainty.

To incorporate geodetic measurements of contemporary deformation into the NZ NSHM 2022, we develop and compare four strain rate maps for New Zealand: (a) the vertical derivatives of horizontal stress (VDoHS) method (Haines et al., 2015; Haines and Wallace, 2020), (b) the BforStrain method based on calculation of body forces using Green's functions (Johnson, 2023), (c) VELMAP (Wang and Wright, 2012; Weiss et al., 2020), and (d) a method based on geostatistics (Maurer and Materna, 2023). We implement each of these methods using the same data set (the campaign GNSS field published by Beavan et al., 2016) and interpolate the results to the same grid so that direct comparisons can be made (grid shown in Fig. 3). Strain rates are incorporated into the NZ NSHM 2022 in two ways: first, as a covariate in the Distributed Seismicity Model (Rastin et al. 2022, 2023), and second, to directly solve for backslip on crustal faults in the New Zealand fault model (Johnson et al., 2022). Both approaches use the velocity field with Hikurangi subduction zone coupling (Wallace et al., 2004, 2012) and sill cooling in the TRHT (Hamling et al., 2015; Hamling, Kilgour, et al., 2022) removed.

Mesh generation. All methods were interpolated into a consistent mesh for comparison and combination. The mesh used is shown in Figure 3 and is the same mesh used for the BforStrain calculation. The nominal node spacing in areas without data is 15 km, but the mesh is refined in regions with more dense data; for example, the node spacing is about 4 km in the Wellington region. The mesh is generated using a MATLAB-based 2D unstructured mesh generator called *mesh2d* (Engwirda, 2014).

VDoHS. The first strain rate field we used was implemented on a New Zealand-wide basis to produce a high-resolution view of tectonic and volcanic deformation (Haines and Wallace, 2020). The VDoHS method, first developed by Haines et al. (2015), assumes a thin elastic plate and solves for a set of body forces that explains the velocity field, then uses those forces to compute strain rates. The velocities and strain rates due to body forces are computed with a finiteelement formulation. Body forces are represented as integrals of spatial stressing rates, which are more spatially compact than strain rates, which are themselves spatial derivatives of displacement fields. The VDoHS method has been implemented in Iceland (Árnadóttir et al., 2018) and has also been adapted for use with GPS time series to resolve transient SSEs and locking processes at the Cascadia subduction zone (Haines et al., 2019).

The solution (Haines *et al.*, 2015) involves discretizing the domain into a finite-element domain and solving for the best-fitting velocity field \dot{u} :

$$\dot{u} = \dot{u}_0 + \sum_i F_i \Phi_i(\vec{x}),\tag{7}$$

in which the velocity basis functions Φ_i are calculated from body forces and F_i are weighting coefficients. The inversion is regularized by minimizing both the norm and the first derivative of the body forces to reduce fitting artifacts. Strain rates are obtained using finite elements and the F_i coefficients.

Haines and Wallace (2020) used a grid of nodes collocated with the GNSS stations. We undertake the same procedure outlined in Haines and Wallace (2020) to derive strain rates from the velocity field, but in the current case, we use the velocity field corrected for sill cooling in the TRHT and coupling at the Hikurangi subduction zone as discussed previously. We generate uncertainty in strain rate components using the velocity uncertainties computed by Haines and Wallace (2020) to calculate realizations of the strain rate field. We generate realizations by multiplying a zero-mean normally distributed vector by the Cholesky factor of a covariance matrix representation of the uncertainty field, using an exponential variogram model to capture spatial correlations in the field, and repeating many times to generate many spatially correlated noise realizations, and then adding those (zero-mean) fields to the original (mean) strain rate components. The

resulting realizations have the same ensemble mean and variance as the original fields.

BforStrain (body force method). Sandwell and Wessel (2016) developed a method similar to the VDoHS method but using the analytical Green's function approach rather than numerical basis functions. As seen from equation (8), the relationship between displacements and body force magnitude is linear and depends on Poisson's ratio. BforStrain (Johnson, 2023) also uses the analytical elastic thin-sheet Green's functions of Sandwell and Wessel (2016) but sets up the velocity field interpolation as an overdetermined inverse problem, similar to the VDoHS method. Body forces are placed at each triangular node, and velocities and strain rates are computed at the triangle centroids. Sandwell and Wessel (2016) provide the mathematical relationship between the vectors of observed velocities, v, and the vector of body forces, f, at all nodes:

$$\mathbf{v} = \mathbf{G}_{\mathbf{v}}\mathbf{f},\tag{8}$$

in which G_{ν} is a matrix of body force Green's functions. Once the velocities are determined, strain rates at the triangle centroids are computed using equation (8). We apply minimum-norm damping (i.e., Tikhonov regularization) and solve the following augmented least squares problem:

$$\begin{bmatrix} \sum_{\nu}^{-1/2} \mathbf{v} \\ 0 \end{bmatrix} = \begin{bmatrix} \sum_{\nu}^{-1/2} \mathbf{G}_{\nu} \\ \alpha^{2} \mathbf{I} \end{bmatrix} f, \tag{9}$$

in which **I** is the identity matrix, α^2 is the damping parameter, and Σ_{ν} is the diagonal matrix of velocity uncertainties. This is a standard approach, with the solution determined directly using the generalized inverse (e.g., Aster *et al.*, 2018; Menke, 2018). Strain rates are computed using body forces, f, and analytical solutions that relate body force to strain rate. We compute body forces and strain rates for a range of values assuming that each value is equally likely. For each of twenty values, we generate 100 realizations of strain rate to compute uncertainties on strain rates.

VELMAP. The VELMAP method was developed by Wang and Wright (2012) based on England and Molnar (1997; see also Weiss *et al.*, 2020) and solves for the velocity field on a triangular mesh, assuming that surface velocities vary linearly within each triangular element (i.e., piecewise linear basis functions). GNSS observations \mathbf{v}_{gnss} are related to the unknown velocities, \mathbf{v} , at the vertices via

$$\begin{bmatrix} \mathbf{v}_{\text{gnss}} \\ 0 \end{bmatrix} = \begin{bmatrix} \mathbf{G}_{\text{gnss}} \\ \alpha^2 \nabla^2 \end{bmatrix} \mathbf{v}, \tag{10}$$

in which G_{gnss} is the design matrix composed of interpolation kernels for GNSS velocities at the triangular nodes, ∇^2 is the Laplacian smoothing operator, the weight of which is controlled by as in the BforStrain method (but see that the BforStrain

method used minimum norm instead of minimum-curvature regularization). A range of values for α was determined using an L-curve approach, picking the central hinge point such that interpolated strain rates were roughly similar to the VDoHS method, and sampling from a range +/-5% of the hinge value. The observations are weighted by the formal uncertainties of the velocities. The velocity in the interior of each triangle is related to the velocity at the vertices using linear interpolation kernels.

To account for uncertainties in the resulting field, particularly related to the choice of smoothing parameter, we perform 1000 bootstrap resamples of the input velocity field and randomly select smoothing factors within 5% of the hinge value, and then invert for grid velocities. To estimate the strain-rate field associated with each velocity realization, we use the spherical approximation equations of Savage *et al.* (2001), which average velocities over connected triangles using a connectivity matrix. The length scale associated with this averaging operation varies but has averages of approximately 0.45° and 0.35° of longitude and latitude, respectively.

Geostatistics. The geostatistical method (Maurer and Materna, 2023) is based on kriging for interpolation, which requires estimation of the spatial structure in the velocity field. We use a Gaussian spatial structure function based on the assumption that the underlying field is both spatially continuous and differentiable (see the supplemental material).

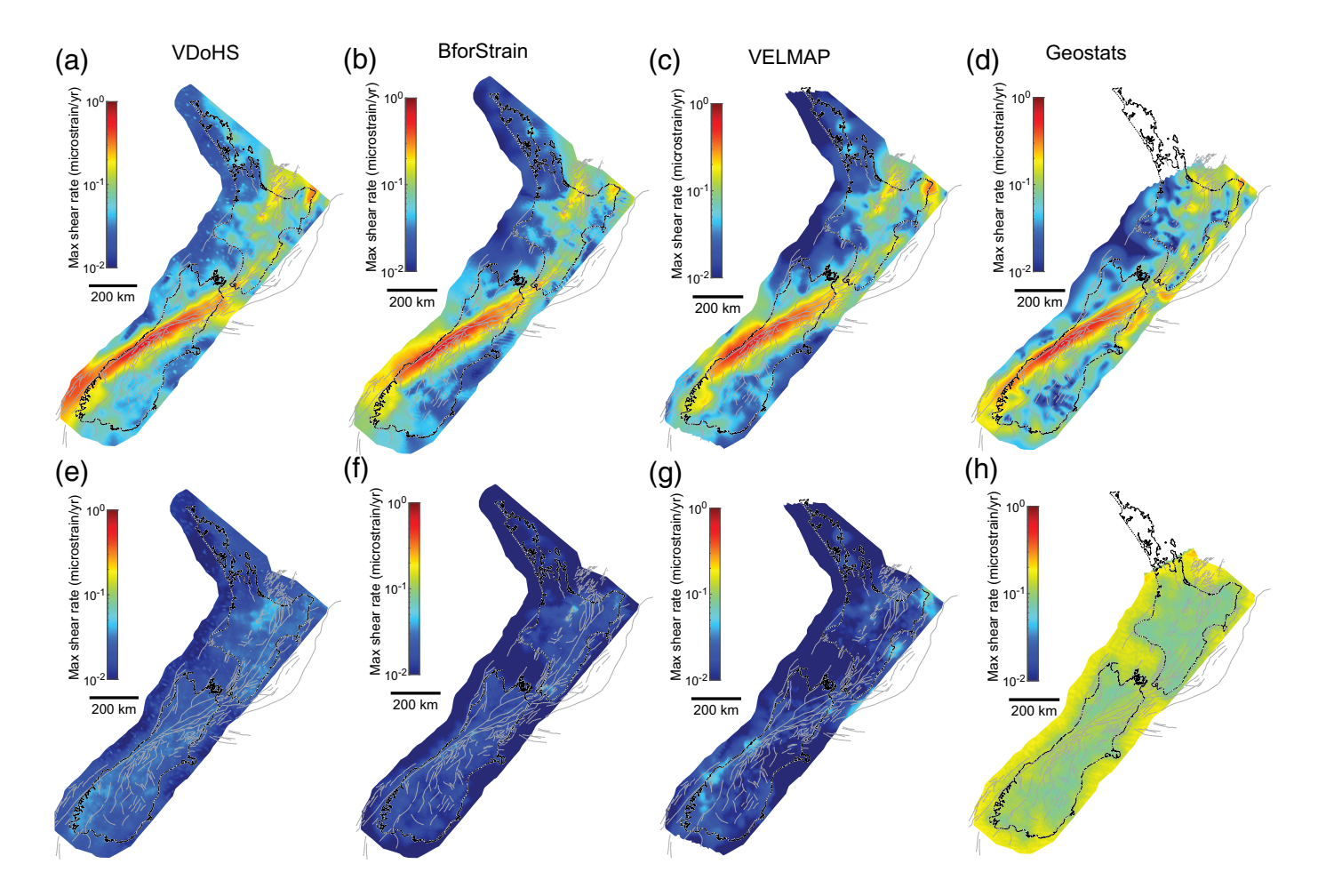
The kriging system solves for optimal (in the least-squares sense) weights λ , in which the estimate at a new location $\hat{Z}(x_0)$ is given by the weighted average of the observations $z(x_i)$, in which the weights are found through solving the ordinary kriging equations using a spatial covariance matrix based on the structure function (Maurer and Materna, 2023).

To account for anisotropy in the spatial correlation length in the New Zealand velocity field, we rotate the velocities into a coordinate system that minimizes the correlation between velocity components. This results in a grid system that does not include the northwest corner of Northland, so the geostatistical method does not show results for that area, which has very low strain rates anyway.

Realizations of the strain rate field can be generated by multiplying the Cholesky factor of the covariance matrix by a vector drawn from a standard normal distribution. This initial field $\mathbf{z}_u(\mathbf{x})$ is "unconditioned," that is, is simply a random field with spatial correlation equal to the GNSS observations but does not necessarily fit the data. Then, in a second step, the realization is conditioned on the observations $\mathbf{z}(\mathbf{x})$ by solving for and adding a component to the field needed to fit the data:

$$\nu_{c,k}(x_0) = \nu_{u,k}(x_0) + \lambda^T (\nu(x_i) - \nu_{u,k}(x_i)),$$
(11)

in which $v_{c,k}(x_0)$ is the kth conditioned realization of the velocity $\mathbf{v} = [v_{\text{east}}, v_{\text{north}}]$, located at x_0 , and λ are weights obtained using the kriging equations.



RESULTS

Figure 4 shows the maximum shear strain rate estimated from each method and the corresponding uncertainty, whereas Figure 5 shows the dilatation rates for each method. All results shown here are using the velocity field with the Hikurangi coupling and TRHT sill cooling signals removed (see discussion in the Data section). This means that the signal from interseismic coupling on the Hikurangi subduction zone has been removed from these plots; we observe that without removal of the coupling signal, much of the southern and eastern North Island is in contraction for all strain rate methodologies (e.g., Figs. S2-S4). Table 1 shows the root-mean-square error (rmse) between the estimated velocities of each model and the GNSS observations, and Figure S5 shows the residual velocity fields for the mean velocities from each method. The models fit the GNSS velocity field at a similar level, with rmse ranging from 1.06 to 1.18 mm/yr, indicating that differences between model strain rates can largely be attributed to methodology differences rather than quality of fit to data. In general, strain rates are similar across all models due to the high spatial density of the used GNSS velocity field. Shear strain rate is concentrated along the Alpine fault, consistent with strike-slip tectonics, and in the north and the east North Island, with diffuse low-rate shear strain (~0.1 microstrain/yr) occurring throughout much of the rest of the country (geographic and tectonic locations are shown

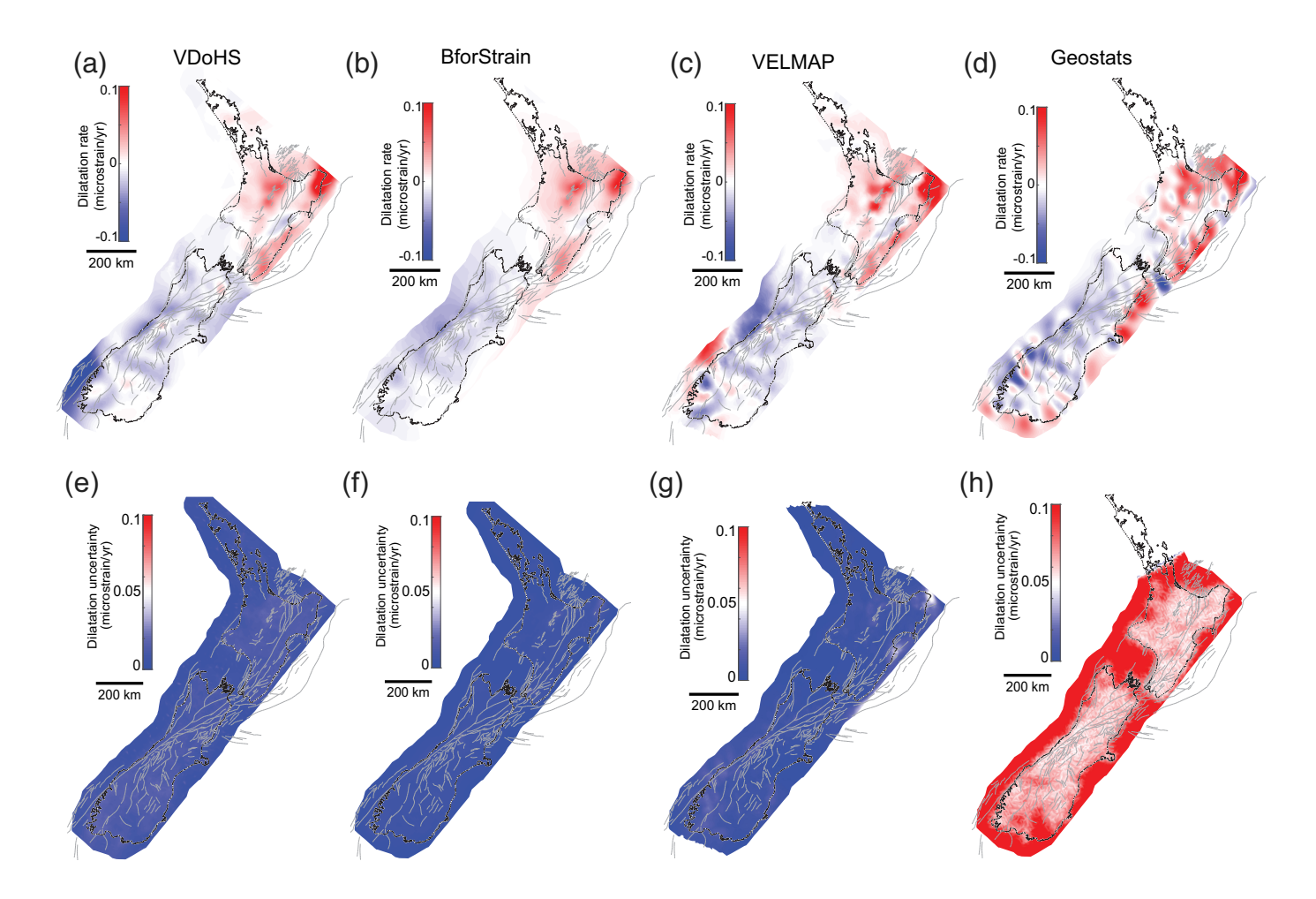
Figure 4. (a–d) Maximum shear strain rate removing the Hikurangi signal and (e–h) corresponding uncertainty for (a,e) the vertical derivatives of horizontal stress (VDoHS) method, (b,f) BforStrain method, (c,g) VELMAP method, and (d,h) geostatistical method. The color version of this figure is available only in the electronic edition.

in Fig. 2). Dilatation rates are primarily contractional in the South Island and extensional in the North Island.

The geostatistical method has significantly higher uncertainties than the other methods, particularly offshore. This is partly because the VDoHS, BforStrain, and VELMAP methods penalize the magnitude of the velocity gradients; thus,

TABLE 1 Misfit Metrics for Each Model				
Metric	VDoHS	BforStrain	VELMAP	Geostats
RMSE	1.09	1.15	1.06	1.18
Weighted rmse	1.60	1.70	1.55	1.80
Reduced χ^2	2.58	2.88	2.39	3.25

RMSE, root-mean-square error; VDoHS, vertical derivatives of horizontal stress. "Weighted rmse" uses the residuals weighted by the data uncertainties. "Reduced χ^2 " is the sum of squared weighted residuals divided by the number of observations. Units are in mm/yr.



away from GNSS observations, the velocities are estimated to minimize strain rate. No matter how uncertainties are propagated from the observations (bootstrap for VELMAP, linear error propagation for BforStrain, etc.), the uncertainty away from the data is low because the gradient penalization reduces the range of allowable models. In comparison, the geostatistical realizations are drawn from a Gaussian distribution with a mean and variance given by the kriging equations. A query point located offshore, with no nearby stations to constrain the velocity there, will have the maximum uncertainty possible based on the geostatistical method, but will have the minimum possible based on the other methods. The two approaches thus represent end-member values for the uncertainty.

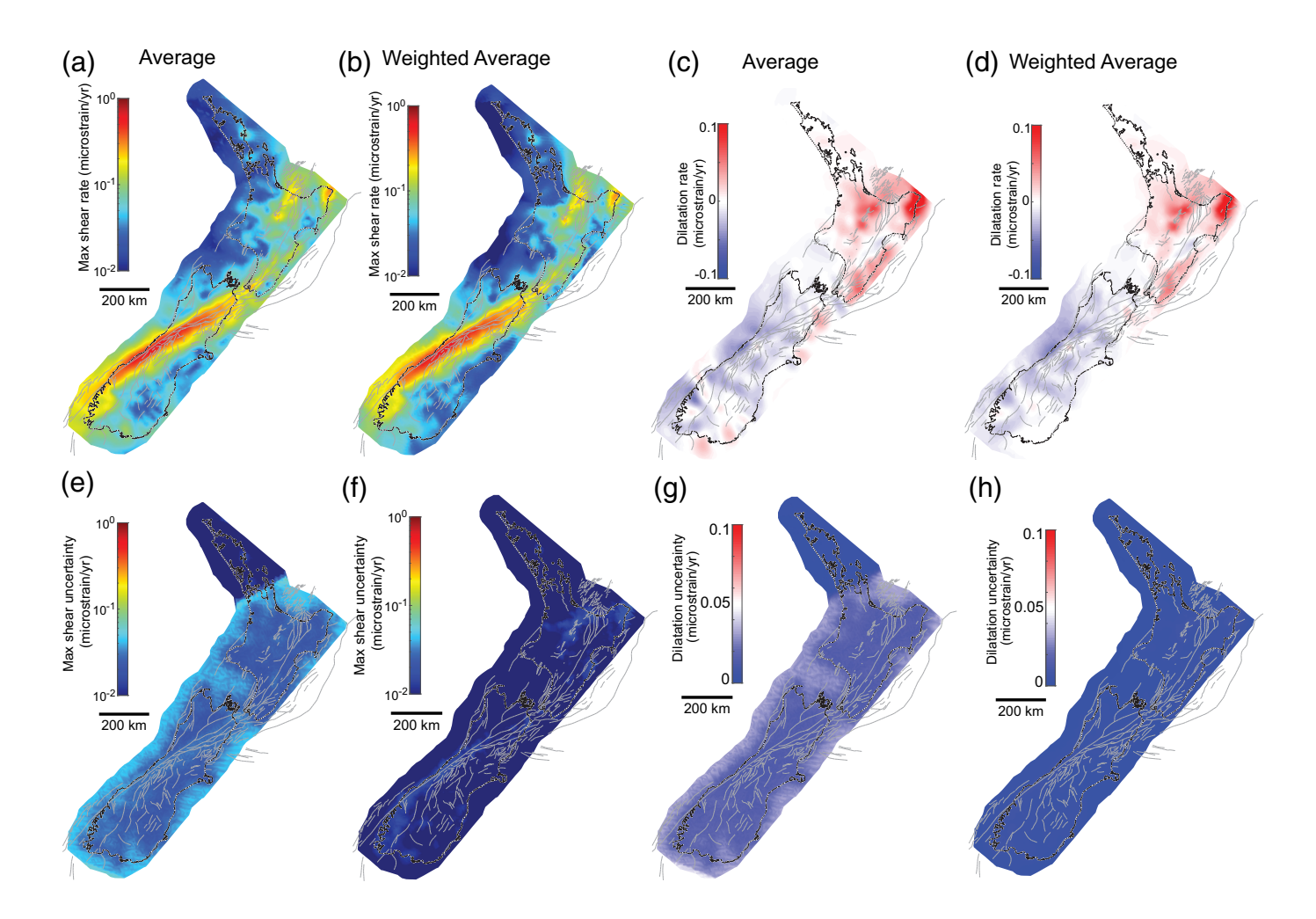
We observe that although dilatation rates in Figure 5 visually appear more variable across methods than shear strain rates due to the color scales, shear strain rates are actually more different between methods. Figure S7 shows histograms of pixelwise epistemic uncertainty (i.e., uncertainty based on the variability between models in Figs. 4 and 5) and demonstrates that maximum shear variability is higher in most places. This is likely because shear strain rates are higher than dilatational rates in most places.

The VDoHS, BforStrain, and geostatistical methods all show primarily extension in the North Island, with minimal contraction along the North Island dextral fault belt

Figure 5. (a–d) Dilatation rate and (e–h) corresponding uncertainty for (a, e) the VDoHS method, (b,f) BforStrain method, (c,g) VELMAP method, and (d,h) geostatistical method. Positive values here imply extension, and negative implies contraction. The color version of this figure is available only in the electronic edition.

(NIDFB; Fig. 2). All methods consistently show extension in northeast North Island, potentially related to normal faulting and/or deep-seated landslides in the Raukumara Peninsula (e.g., Chanier et al., 1999; Dimitrova et al., 2016; and references therein) or to residual strain from incorrect modeling of the subduction zone (Johnson et al., 2022), although the strain signal is present in the uncorrected maps (Figs. S2–S4). All four strain rate maps show largely contraction throughout the South Island, consistent with thrust and transpressional tectonics, but there is some disagreement between models at and below ~100 km spatial scales, depending on the relative smoothness of the models.

We calculate the mean strain rate field across the four methods using two approaches (Fig. 6). First is using equal weights for all four methods (i.e., ordinary average), except in Northland, where the geostatistical method does not provide strain rates and we weight equally the other three methods. The uncertainties are similarly weighted and combined using



standard linear error propagation (Fig. 6a,c,e,g). The second method of combination is to weight each method by the inverse of its own uncertainty, normalized such that the weights sum to one (Fig. 6b,d,f,h). This has the disadvantage that if the uncertainty is underestimated for a method, the weight assigned to that method will be disproportionately high in the result, but the benefit is that uncertainties are consistently propagated to the combined solution. Uncertainty varies spatially, so the weights for a given method vary spatially across the domain. Average weights are approximately 0.141, 0.432, 0.420, and 0.005 for the VDoHS, BforStrain, VELMAP, and geostatistical methods, respectively. Figure 6 shows that in general there is relatively little difference in the combined strain rates between the two methods of weighting, which is a reflection of the overall similarity between models, whereas the uncertainties are quite different due to how the large geostatistical uncertainties get handled by the different weighting schemes.

Figure 7 shows the standard deviation of the maximum shear and dilatation rate calculated from the four models, that is, taking the standard deviation across the top row of Figures 4 and 5. This measure of variability could be considered to be one estimate of the epistemic uncertainty, capturing variability that is due to the different modeling assumptions made by each

Figure 6. Average (a,b) maximum shear strain rate and (c,d) dilatation rate with (e—h) uncertainties obtained by combining the four strain-rate methods. Panels (a,c) and (e,g) are obtained using equal weights on each method, and panels (b,d) and (f,h) are obtained by weighting each map by its uncertainty. The color version of this figure is available only in the electronic edition.

method. Unsurprisingly, the epistemic uncertainty is largest in off-shore regions.

Figures 8–10 show zoomed-in subsets of the total strain rate maps to highlight some interesting features in each region of New Zealand. In the areas of Southland and Otago and in the areas of Marlborough and Canterbury (Fig. 8), the majority of shear strain rates can be attributed to interseismic locking on the Alpine fault and the Marlborough fault system to the north-northeast (Wallace *et al.*, 2007, 2012). However, as also discussed in more detail in Haines and Wallace (2020), there are nontrivial strain rates on north-northeast– to south-south-west–striking faults south and east of the Alpine fault that contribute to the wide belt of shear strain in the region. Moderate shear strain rates also occur along the complex contractional and strike-slip fault systems south of the Hope fault in the north Canterbury region. Contraction occurs in a "striped"

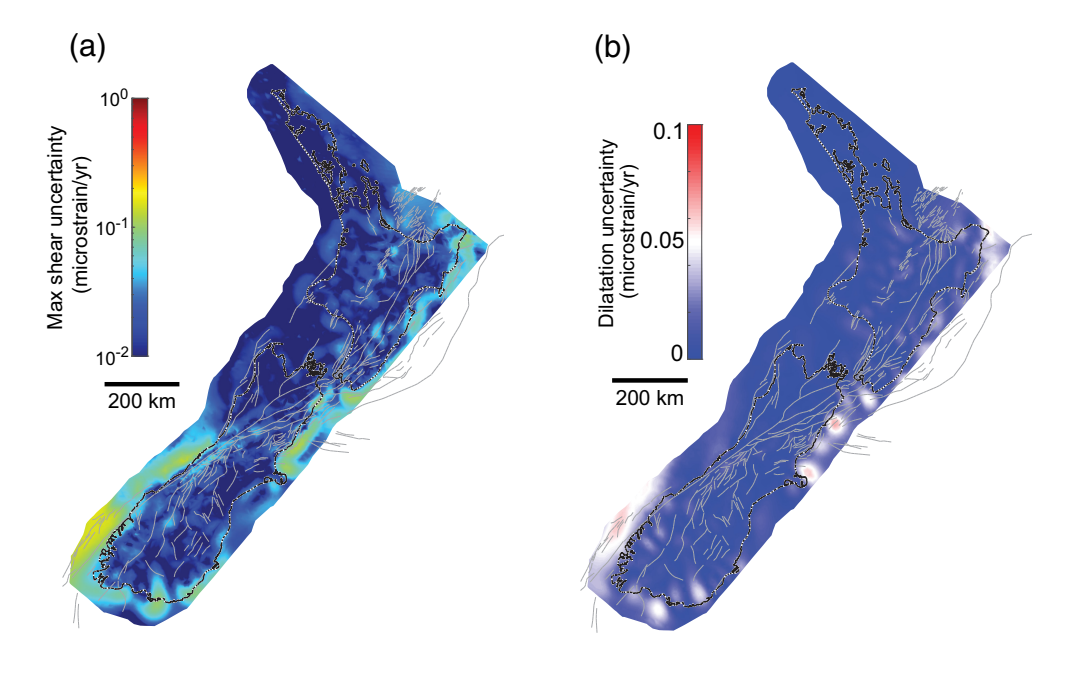


Figure 7. Standard deviation of the (a) maximum shear strain rate and (b) dilatation rate of the four models shown in Figures 4 and 5, calculated using equal weights. We interpret these plots as representing the epistemic uncertainty in strain rate. The color version of this figure is available only in the electronic edition.

pattern that is generally consistent across all four methods but may be an artifact due to the spatial distribution of the observations in Otago and Southland, which is sparser than in other regions of the country. Similar artifacts due to irregular data spacing were pointed out by Baxter *et al.* (2011).

Figure 9 shows zoomed-in results for central New Zealand (i.e., the upper South Island and lower North Island). The localized zone of maximum shear strain rate decreases in magnitude gradually from the Alpine fault system to the south, through the Marlborough fault system in the middle of Figure 9, and then north through the Wellington region in the North Island. This zone of highest maximum shear strain rate decreases in magnitude through the northeast end of the South Island and into the North Island. Spatial oscillations in dilatation rate are also visible in this region, primarily offshore. This effect may also partly be due to the spatial aliasing of gridded data, as explored in Baxter et al. (2011). This particular area of oscillation is present to some degree in all the models, which is why it shows up in the mean model here, but appears most strongly in the geostatistics and VELMAP models, which do not penalize strain away from observations.

Figure 10 shows results for the North Island region. The shear strain rates are lower than in the South Island, on the order of 0.1 microstrain/yr and less. The strain is distributed broadly across the North Island, including within the TRHT, the NIDFB, and somewhat along the eastern coast. The dilatation rate is primarily extensional; we see here that we have removed the impact of subduction through the block modeling.

DISCUSSION

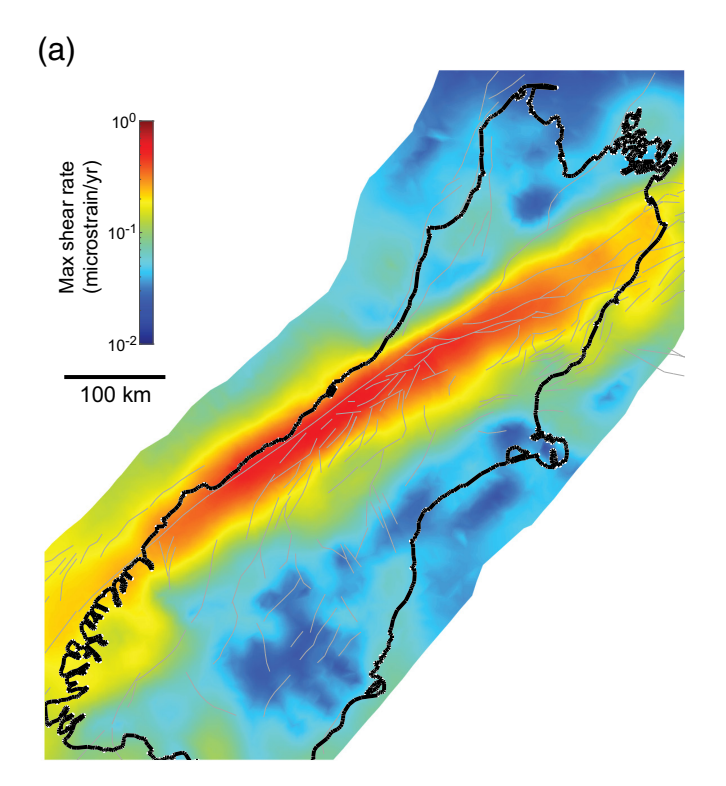
Implications for seismic hazard in New Zealand

Figure 11 shows the integrated Kostrov moment rates (Savage and Simpson, 1997) for each realization. Figure S6 shows spatially averaged dilatation and maximum shear strain rates (i.e., per realization) for all realizations of strain rate for each of the four methods (see Text S3). The moment rate distributions are calculated using fixed geometry and shear modulus (30 GPa); obviously, the real parameter values will vary spatially, but fixed spatial variations in shear modulus and depth will only influence the mean values, not the variance across realizations. Total moment rate using a locking depth of 15 km has a range

of $0.7-2.2 \times 10^{19} \text{ N} \cdot \text{m/yr}$ including all points in our mesh, or $0.64-1.48 \times 10^{19} \text{ N} \cdot \text{m/yr}$ using only on-shore points (Fig. 11; these values do not include the contribution from Hikurangi). This corresponds to approximately one $M_{\rm w}$ 7 earthquake every 1.6-4.5 yr. Assuming a locking depth of 20 km results in a range of $0.93-2.93 \times 10^{19} \text{ N} \cdot \text{m/yr}$ using all points or $0.85-1.97 \times 10^{19} \text{ N} \cdot \text{m/yr}$ for onshore points only. In comparison, there have been 11 $M_{\rm w}$ 7+ earthquakes in the general study area in the last 100 yr (Table S1; GNS Science, 2022) with a total moment release of approximately $\sim 2 \times 10^{21}$ N·m, or an average rate of $\sim 2 \times 10^{19}$ N·m/yr over the same 100-yr period. This comparison (which ignores the Hikurangi subduction interface) is quite different from the situation in southern California, in which historic seismicity is at best barely keeping up with the geodetic moment rate and may be as much as a full $M_{\rm w}$ 8 event behind the geodetic rate (Maurer et al., 2018). This difference between the two major fault systems may be due to differences in the relative time during each major fault's earthquake cycle (~312 yr for the Alpine fault compared with 166 yr for the San Andreas).

Implications for strain rate estimation

Every strain rate estimation method needs to estimate or assume some value for the relevant spatial correlation length scale; that is, the length scale at which a given GNSS velocity, for example, has relevance for the estimation of velocity at an unobserved location. For example, variogram analysis shows that the correlation length scale for GNSS velocities in New Zealand is around 250 km (Fig. S7). In most areas of New



Zealand, any point will likely have many GNSS stations within 250 km, so the estimation is well constrained and the different methods are similar. Our results show that the differences between the strain rates are largest in areas with sparse or no data, as expected. Maurer and Materna (2023) showed that there are two cases in which strain rate methods tend to differ from one another: cases in which there is little or no data (e.g., Southland/Otago in New Zealand), and cases in which there is both more data than average and higher strain rates than average (e.g., northern Alpine fault, TRHT). The reason for the disagreement in the second case arises because of how different methods handle short-wavelength variability in the limited areas that have much more data than the region-wide average (Maurer and Materna, 2023).

A related question is, to what extent can the estimated strain rates for an individual method be trusted as reliable? Our work demonstrates that in areas without sufficiently dense observations ("sufficiently dense" being a function of the spatial length scale involved; see Maurer and Materna, 2023), estimation methods can produce quite different results due to the different assumptions made in each case. In locations with little or no data, each method provides some type of "best estimate," in which "best" is defined differently by each method. For example, geostatistics provides the provably best estimate in a leastsquares sense when the spatial correlation function is known, whereas the BforStrain and VDoHS methods provide the smoothest strain rates that fit the observations, given their other constraints. These represent different philosophical approaches to the estimation problem. This also extends to choices made for a given method; for example, the particular geostatistics implementation we used for this study uses a

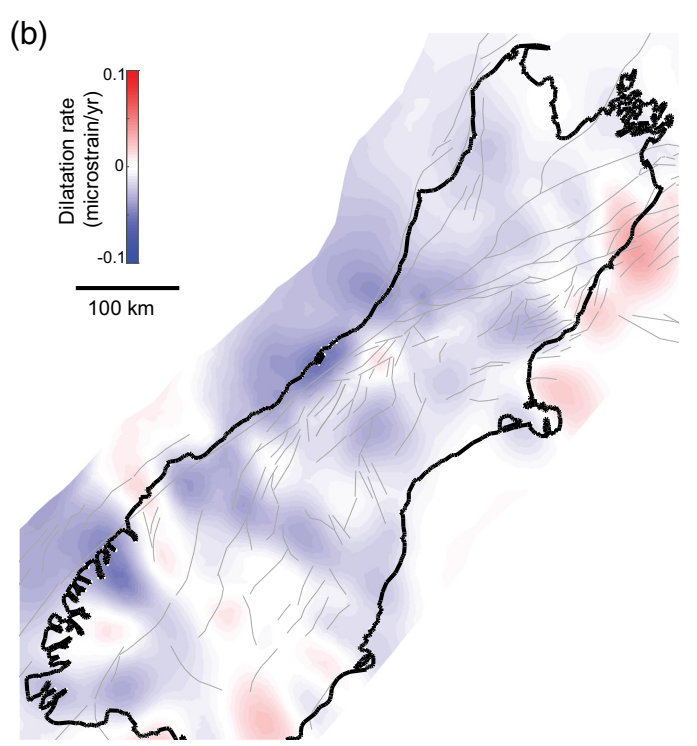


Figure 8. Zoom-in on (a) maximum shear and (b) dilatation results for the South Island, including the Southland and Marlborough/Canterbury regions. The results shown are averaged across all four models with equal weights. The color version of this figure is available only in the electronic edition.

single correlation length scale, whereas in reality the appropriate length scale likely varies spatially based on the particular source of strain. These differences are a motivation for averaging, which functions in a similar way to a low-pass filter in which the cut-off wavelength is dependent on station spacing. The net effect is that averaging strengthens signals that are present in all methods and damps out signals that are not, and it also provides an estimate of the epistemic uncertainty based on variability between methods. This also means that averaging tends to smooth out details that may be present in some individual methods but not others; such short-wavelength features may be real but cannot be reliably estimated based on the existing observations.

Finally, we see that the geologic processes responsible for the strain rates we show in this study may not all be tectonic. We rely on a high-quality, previously vetted velocity field, from which we have removed obvious nontectonic velocities related to volcanic cooling in the TRHT. This reduces, but does not eliminate, the possibility of other nontectonic strain sources in our results. Averaging multiple models does not eliminate this issue because all methods use the same velocity field, and the epistemic uncertainty estimated by taking the standard deviation of all the models does not include the uncertainty arising from potential nontectonic sources of strain rate (Fig. 1b). In other words, our work directly addresses only

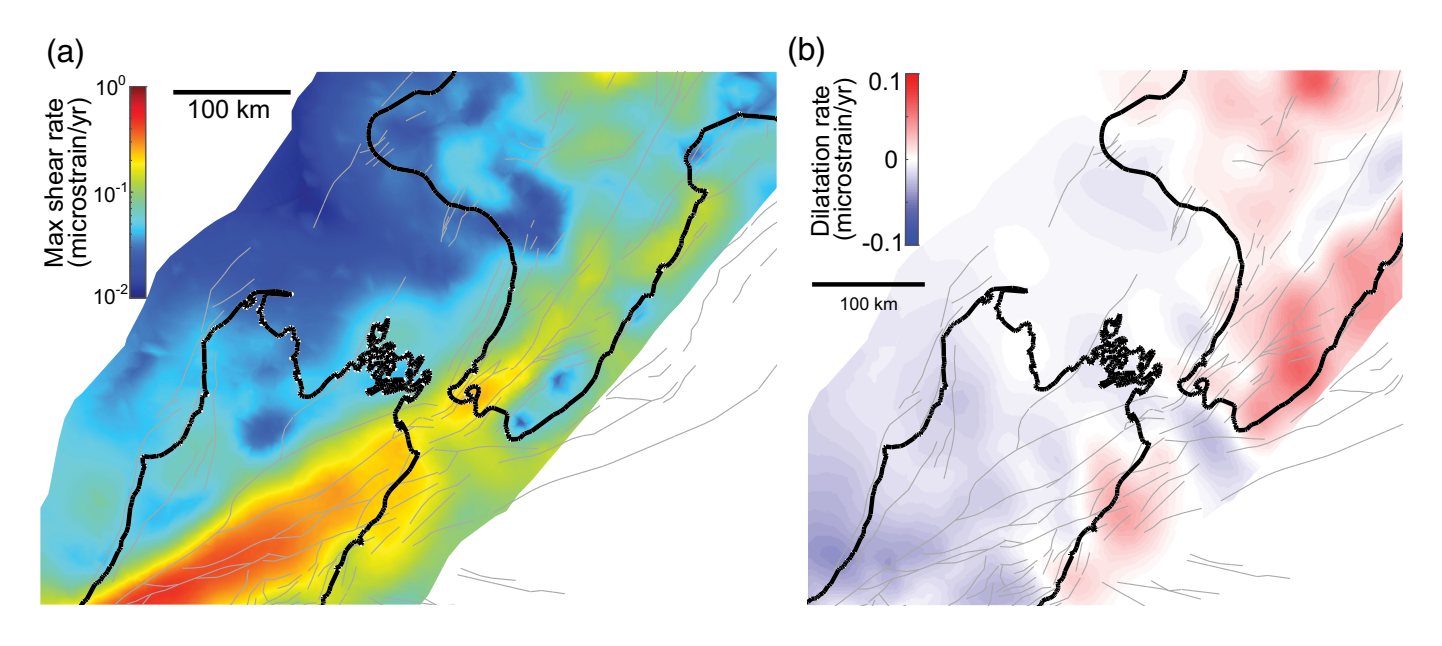


Figure 9. Zoom-in of (a) maximum shear and (b) dilatation results for central New Zealand. The results shown are averaged across all four models with

equal weights. The color version of this figure is available only in the electronic edition.

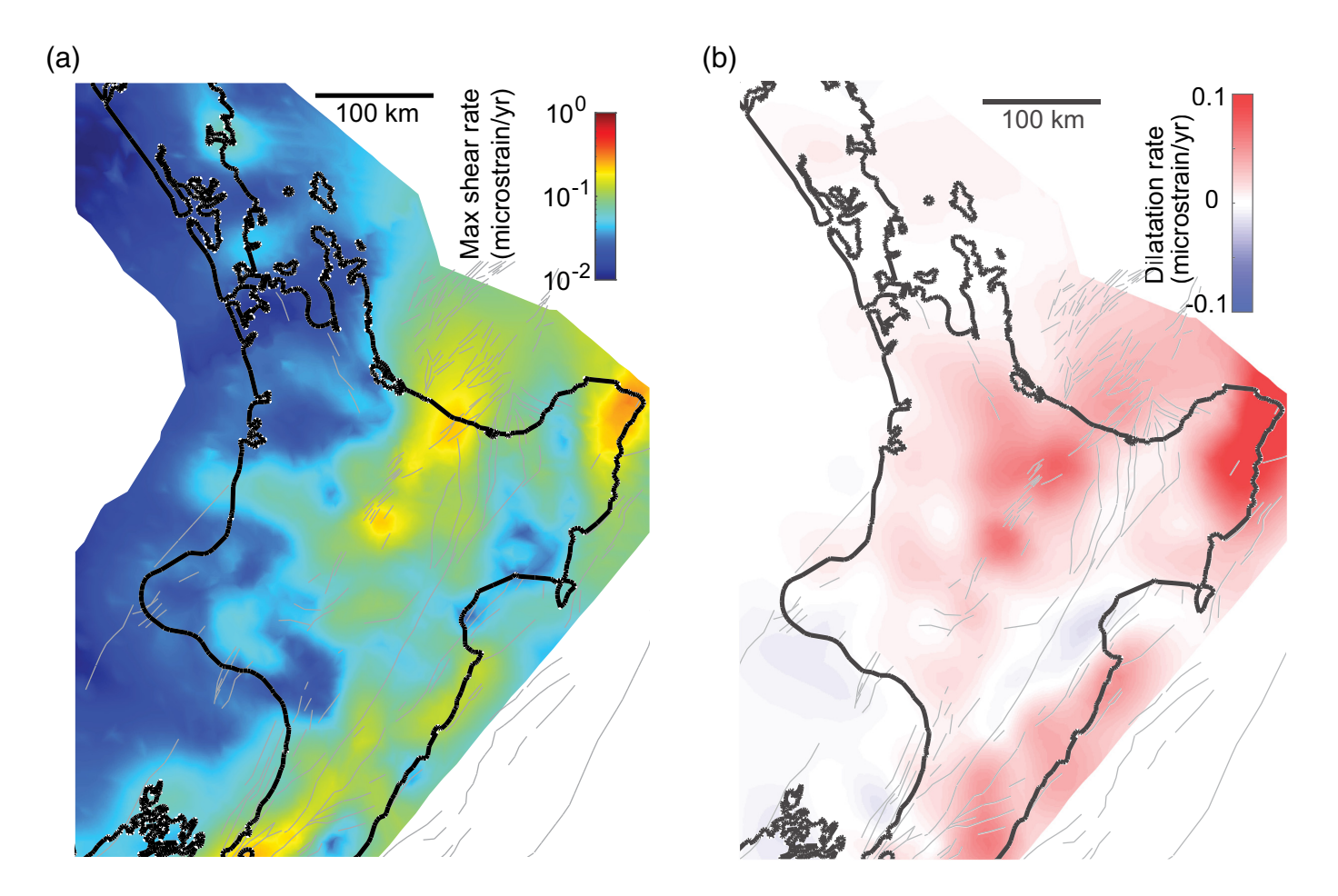


Figure 10. Zoom-in of (a) maximum shear and (b) dilatation results for the North Island. The results shown are averaged across all four models with

equal weights. The color version of this figure is available only in the electronic edition.

Volume 114 Number 1 February 2024 www.bssaonline.org

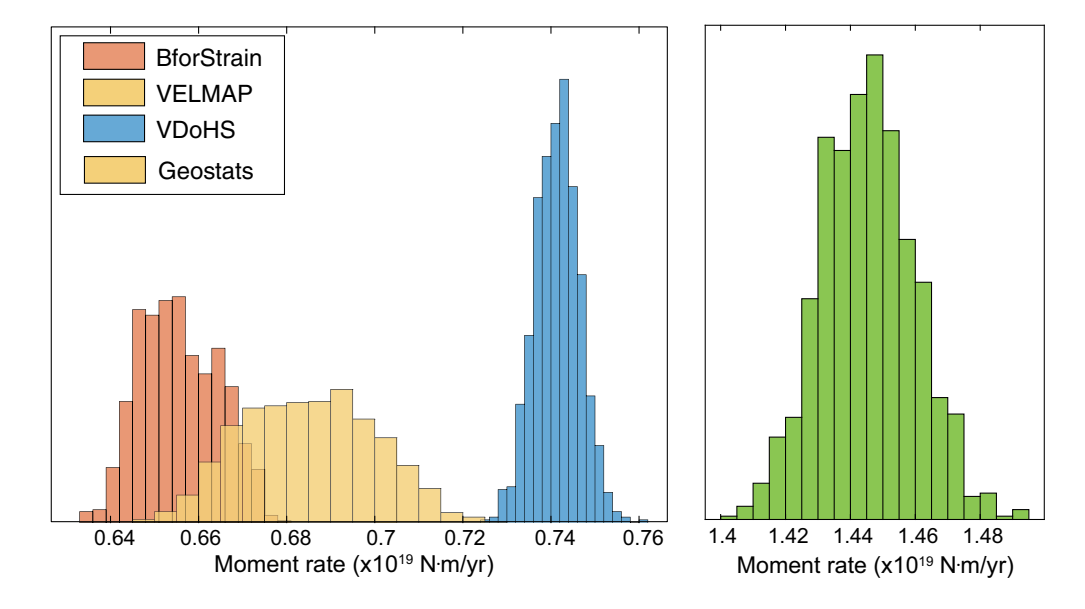


Figure 11. Total moment rate for the realizations of each model using equation (5), assuming a locking depth of 15 km and a shear modulus of 30 GPa. These moment rate histograms are calculated using only points on land. The color version of this figure is available only in the electronic edition.

the first two types of uncertainty shown in Figure 1b. We assume the third type (numerical uncertainty) is minimal for sufficiently fine grid spacing, and we have tried to minimize the potential for the fourth type (uncertainty in source or cause) using a vetted velocity field and removing the TRHT signal. However, there is nothing inherent in comparing or combining multiple strain rate methods that provides any sensitivity to this last type of uncertainty.

Implications for strain rate uncertainty

We have developed a suite of strain rate models, all of which fit the data at approximately the same level (Table 1). Analysis of the results from the different strain rate methods shows that there are strong similarities as well as interesting differences among the four strain rate models shown in Figures 4 and 5. Fit to the data is similar across all methods (Table 1) and uncorrelated with model roughness, with VELMAP having the lowest misfit and the geostatistical method the highest. Differences in strain rate offshore reflect the different method assumptions but also reflect differences in boundary condition assumptions. Comparing Figures 4-6 to Figure 7 shows that differences among methods are in general smaller than the uncertainty estimated for a given method. Figure 12 shows the coefficient of variation for the mean strain rate model (Fig. 6e and 6g divided by Fig. 6a and 6c, respectively). In most areas onshore, the magnitude of the strain rate exceeds the uncertainties, with the exception of the Otago area and parts of Northland.

Figure 13 shows the ratio of the epistemic uncertainty to the aleatory uncertainty (Fig. 7a and 7b divided by Fig. 6e and 6g, respectively). This figure illustrates that epistemic uncertainties

are large relative to aleatory uncertainty in many regions, especially locations with a higher total strain rate. For the dilatation rate in particular, epistemic uncertainty exceeds aleatory almost everywhere. The conclusion that the uncertainty related to the type of interpolation or solver method can be larger than the formal uncertainties of a particular method demonstrates importance of averaging multiple methods to compute strain rates. Variability among methods occurs below the scale of station spacing, as expected, but also tends to be higher in areas where velocity gradients are particularly high (e.g., Alpine fault zone, TRHT,

NIDFB). These areas of strong gradients are impacted by the different assumptions of the different methods and result in some of the largest differences among methods. This likely occurs because the methods are all tuned to a single set of parameters that, in reality, may vary spatially across the region (Maurer and Materna, 2023). This means that in areas of higher-than-average gradients, the spatial interpolation parameters chosen for the whole area may not be optimal for estimating the locally high strain rates, and thus these areas do not necessarily get well resolved even with dense station spacing.

We can further analyze the variability among methods by removing the mean strain rate (averaged across all methods) from each individual model and considering the residual strain rates. Figure 14 shows the residual maximum shear strain rate and dilatation rate (removing the equally weighted average). Unsurprisingly, the largest deviations from the mean strain rate field occur offshore where there are no data constraints and, to a lesser degree, within the high strain rate belts (the Alpine fault zone and the NIDFB). The BforStrain and VDoHS models have the lowest deviations from the mean, whereas the geostatistical model shows the largest degree of variability, and the VELMAP model also shows some systematic deviations in maximum shear strain rate. The geostatistical method also shows smaller scale variability, in the South Island especially, which is at a similar scale to the station spacing. This is true of all the maps; there is some degree of variability that is at or below the scale of the station spacing, implying that different methods for strain interpolation are not consistent at the smallest scales.

We have presented the results of four strain rate methods without commenting so far on which, if any, are the "best" in

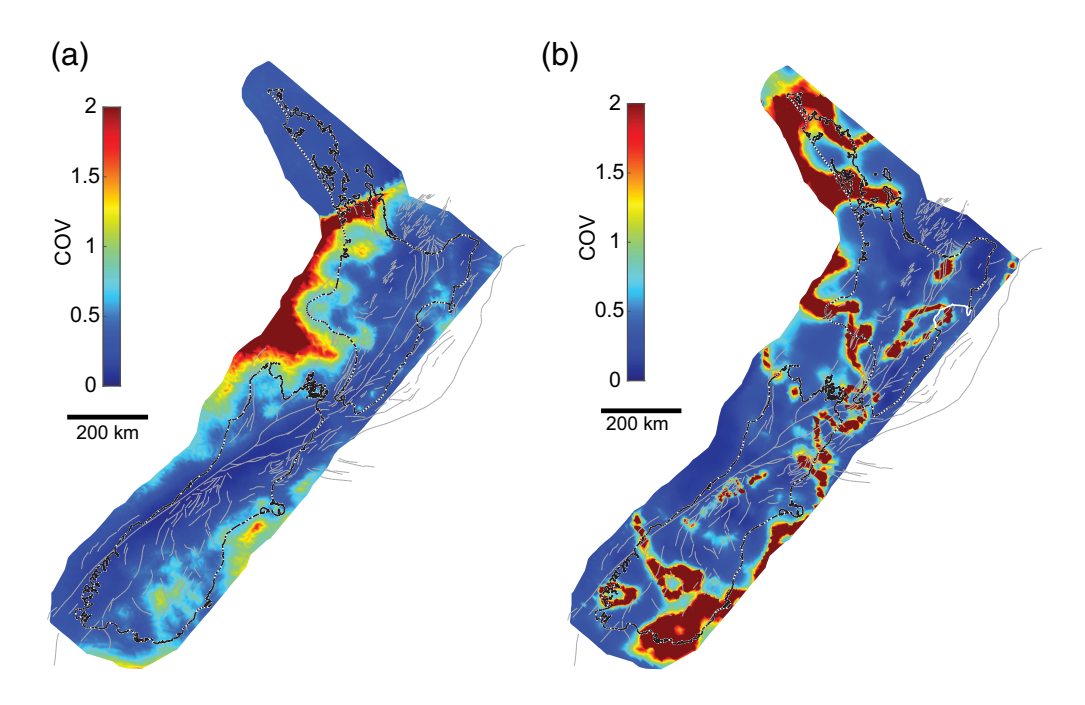


Figure 12. Coefficient of variation (COV), dividing the simple (i.e., unweighted) standard deviation by the average. (a) Maximum shear COV (Fig. 6e divided by Fig. 6a). (b) Dilatation COV (Fig. 6g divided by the absolute value of Fig. 6c). The color version of this figure is available only in the electronic edition.

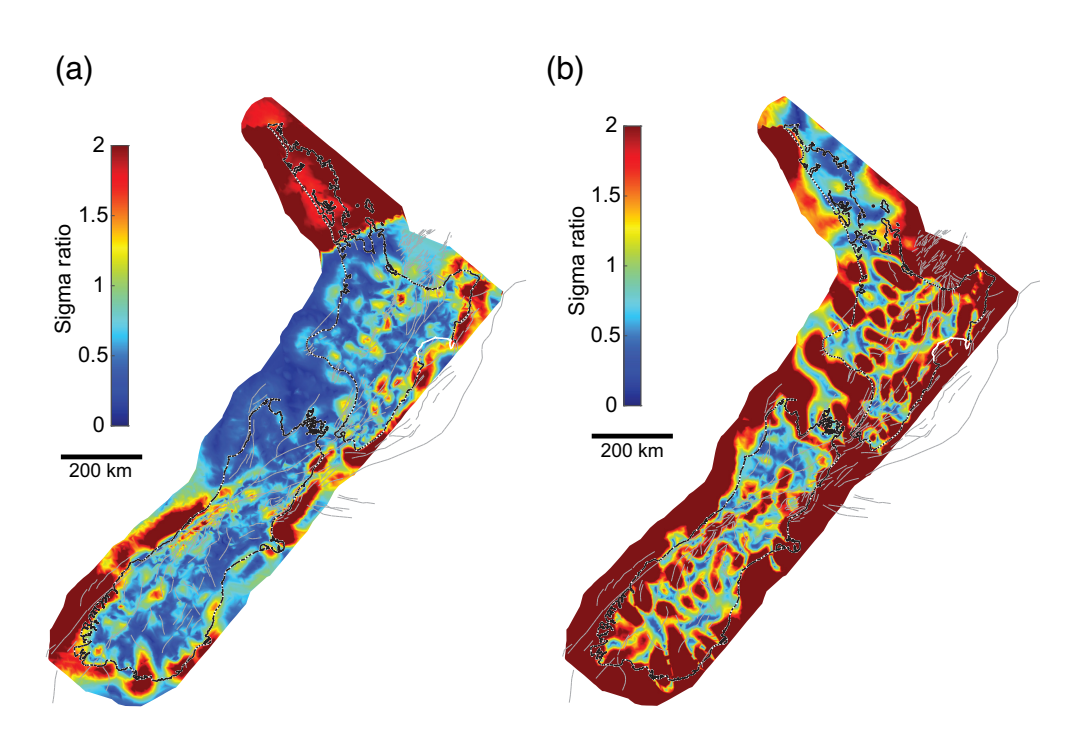


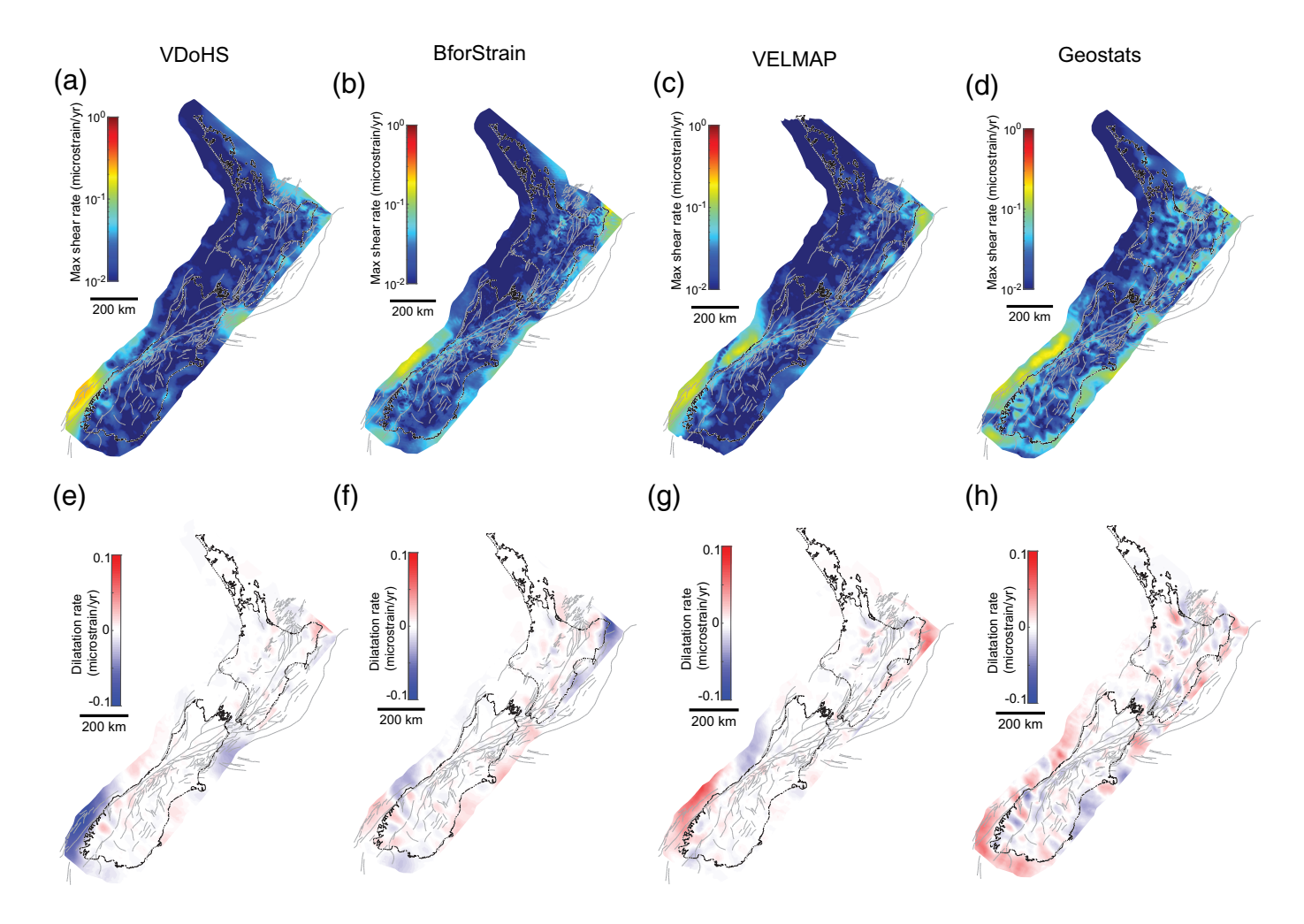
Figure 13. Ratio of epistemic uncertainty over aleatory uncertainty for the simple average maps (Fig. 6e,g). (a) Maximum shear ratio (Fig. 7a divided by Fig. 6e) (b) Dilatation ratio (Fig. 7b divided by Fig. 6g). The color version of this figure is available only in the electronic edition.

terms of most accurately reflecting true tectonic strain rates. Clearly, the differences between methods are, in some cases, larger than the uncertainty calculated for each method. We

propose that such differences reflect real variability (uncertainty) that is allowed by the observations, and as such, averaging multiple methods likely represents a more robust estimate of the strain rate than any one method can provide alone. In addition, accounting for uncertainty through probabilistic weighting of multiple methods avoids biasing the results of derived quantities such as the total moment rate, which could occur when only using one method. Thus, the answer we propose is to average results derived from multiple defensible methods together and propagate errors to estimate strain rate rather than seeking a single "best" method.

As seen earlier, the uncertainties in strain rate presented here only reflect the velocityfield and interpolation uncertainties (Fig. 1b). As seen in the Implications for seismic hazard in New Zealand section, uncertainty related to the interpretation of how much of the strain rate shown in this study can be related to strain accumulation on faults (as reflected in Fig. 1a) is not quantified by our results. The issue of how much strain is explainable in terms of fault coupling is further investigated in a companion study (; K. Johnson et al., unpublished manuscript, see Data and Resources). Strain due to non tectonic sources, such as subsidence due to groundwater withdrawal, largescale landslides, and volcanic deformation, adds additional uncertainty to the interpretation of strain rate signals. Some of

these signals have short spatial wavelengths compared with those of faulting-related strain, but modeling is required to fully separate signals from different sources.



"Strain rate style" and comparison with geologic faulting style

Strain rate "style" can be inferred from strain rates using an eigenvector decomposition to determine principal strain-rate directions and magnitudes (equation 6) and can be compared to faulting style. Strain rate style may not reflect faulting style everywhere because the instantaneous interseismic strain rate does not necessarily reflect the absolute stress in the crust; also, we have removed the contribution of locking on the Hikurangi subduction zone to the strain rate field, which explains the discrepancy in this location between geologic faulting patterns and the surface strain rate. Faulting style from geologic information is shown in Figure 15 (Seebeck et al., 2022, 2023). Figure 16 shows the geodetically derived strain rate style (contraction, extension, shear). Strain rate tensors are represented as wedge diagrams, in which the width of the wedge represents the 2-sigma uncertainty in direction propagated from the uncertainties in the strain rate components, and style is shown based on the mean orientations. Red symbols indicate extension, and blue symbols indicate shortening rates. At long wavelengths, the methods mostly agree with the geologic faulting style, but there are significant differences at short to intermediate wavelengths (~100 km and less). The Alpine fault zone region shows a consistently strike-slip faulting-style strain rate, whereas strain

Figure 14. Residual (a–d) maximum shear strain rate and (e–h) dilatation rate for each of the four methods after removing the mean (equal weights) model. The color version of this figure is available only in the electronic edition.

rates in other regions display different and even opposite faulting styles to the geologic model (e.g., Otago and Southland regions). The geostatistics and VELMAP methods tend to be more spatially variable and differ from the geologic faulting style more significantly than the VDoHS and BforStrain methods, both of which have smoother strain rates. This implies that the epistemic uncertainty discussed earlier has implications for both the magnitude and the implied faulting style of the strain rates.

Recommendations and future directions

Based on what we learned from comparing strain rates in this study, we can make a series of recommendations for the use of the strain rate maps in future seismic hazard models:

1. Strain rate uncertainty can be estimated using both propagation of errors in individual methods (aleatory) and by comparing ranges of estimates from varied methods

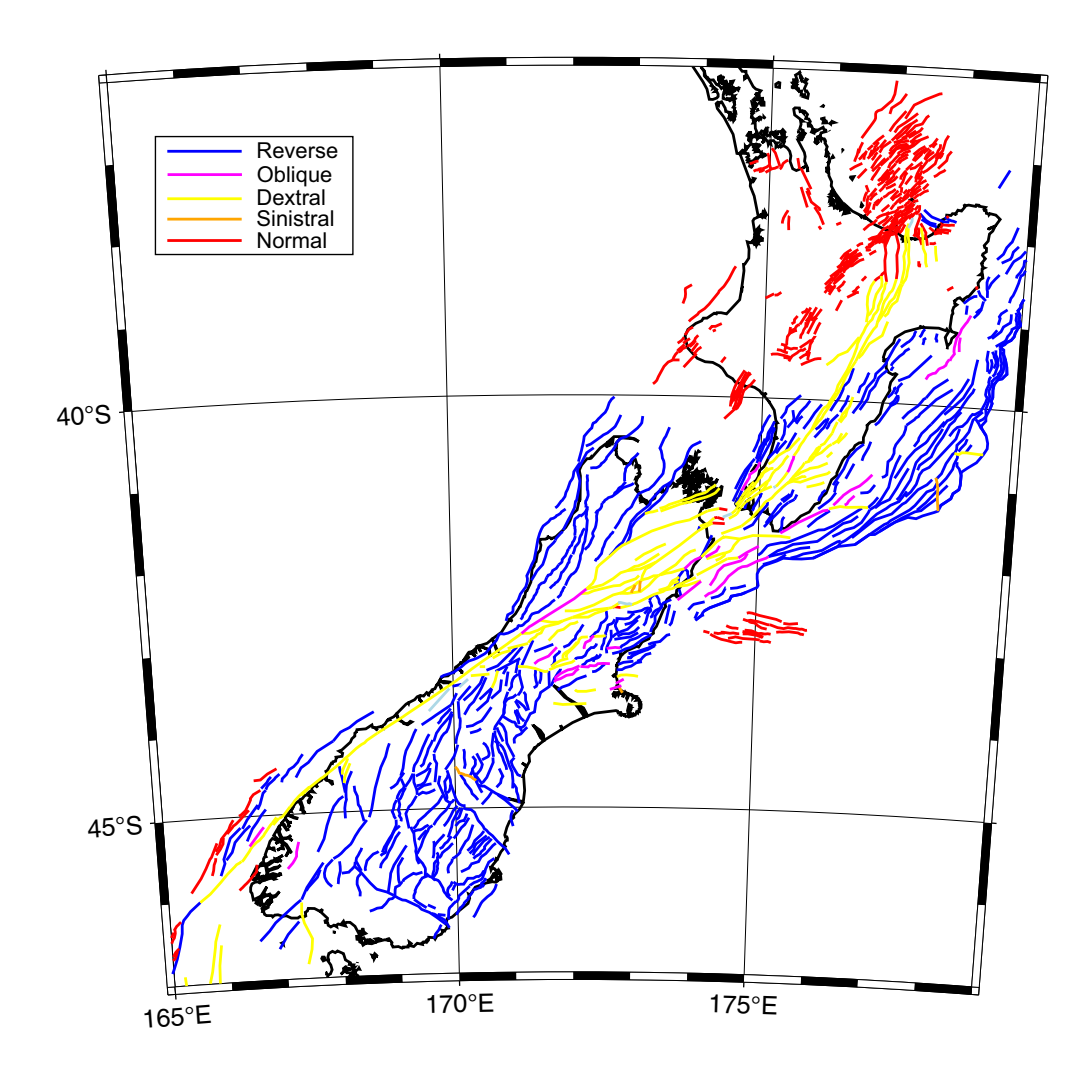


Figure 15. Faulting style based on geology for the faults in the New Zealand Community Fault Model v.1.0 (Seebeck *et al.*, 2022, 2023). The color version of this figure is available only in the electronic edition.

(epistemic). Epistemic uncertainties in strain rate should not be neglected in uncertainty analysis, and in many places in New Zealand, where spatially dense geodetic observations are available, they are larger than aleatoric uncertainties. By comparing multiple defensible strain rate methods, strain rate uncertainty can be quantified and propagated through the equations for derived quantities such as the moment rate needed for seismic hazard calculations (see also Maurer and Materna, 2023).

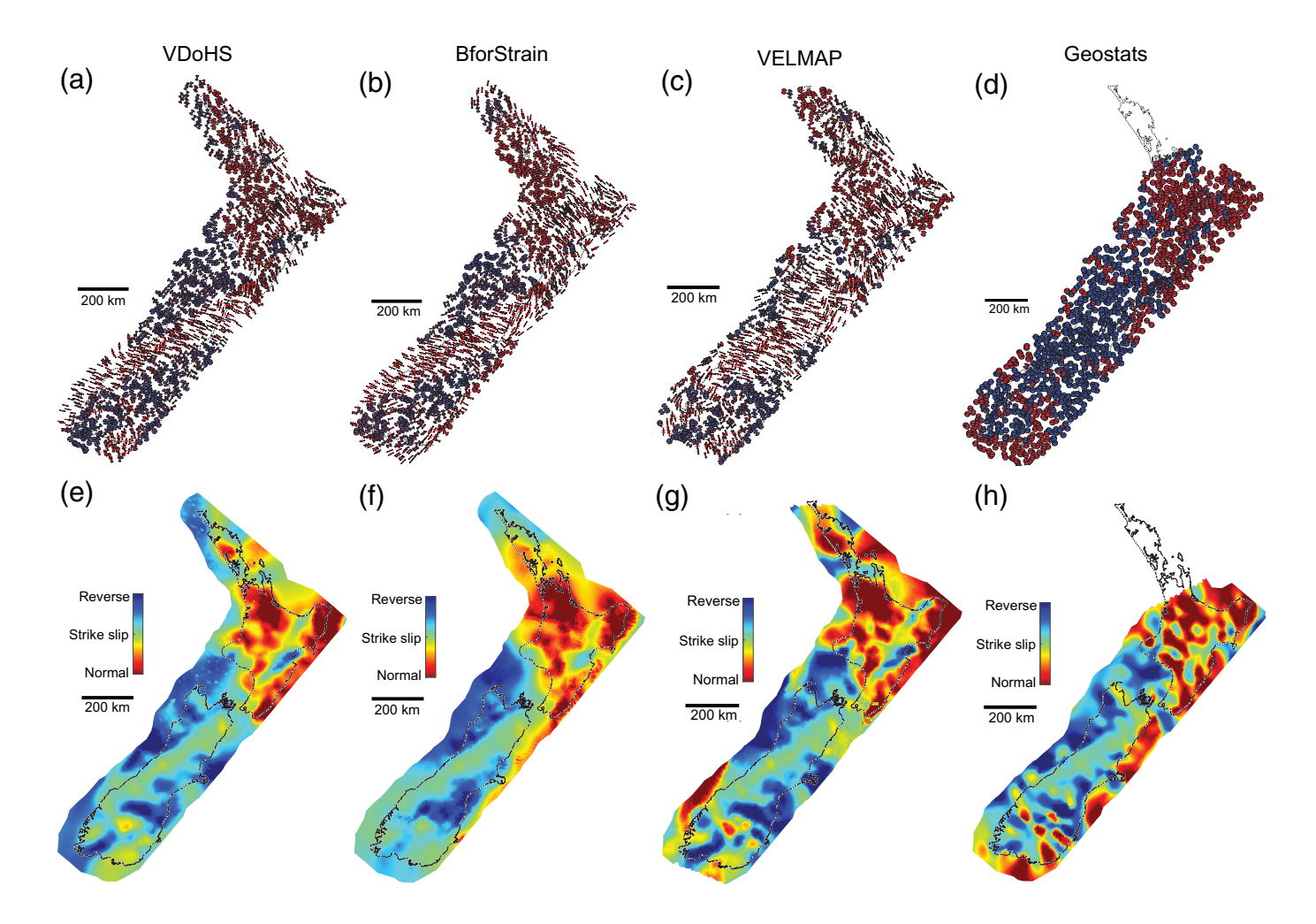
2. Although incorporating geodetic data in the form of strainrate maps into the NZ NSHM 2022 fault source model represents a significant advance on what has been done in previous versions of the NZ NSHM, there are still many improvements that could be made in future versions of the NZ NSHM. For example, we separated out the contributions to strain accumulation due to coupling on the Hikurangi subduction interface from the contribution due to crustal faults using a block model for Hikurangi coupling. We did this without consideration of the uncertainties in modeled

strain rates due to subduction coupling, and thus the epistemic uncertainties near the Hikurangi interface are likely underestimated. Future models should be implemented with crustal and subduction interface contributions to the strainrate field estimated simultaneously (rather than separately). Other strain rate methods should be explored (e.g., Tape et al., 2009; Shen et al., 2015; Kreemer et al., 2018); in particular, methods that allow for automatic multiscale estimation of spatial parameters should also be considered (e.g., Tape et al., 2009; Shen et al., 2015). Maurer and Materna (2023) provide an opensource code for systematic comparison of a subset of strain rate methods; further development along these lines would assist practitioners in the implementation of multiple methods.

3. Interferometric Synthetic Aperture Radar (InSAR) observations should be integrated into standard GNSS-

only strain rate analyses. An InSAR-based view of interseismic deformation in New Zealand shows promise (Hamling, Wright, et al., 2022), and future geodetic strain rate models to underpin fault-slip inversions should incorporate these data as well. Other studies have looked at using InSAR for strain rates (e.g., Tymofyeyeva and Fialko, 2018; Song et al., 2019; Wang et al., 2019; Weiss et al., 2020; Franklin and Huang, 2022), but more work remains to be done to fully integrate and use it with GNSS for strain rate estimation.

4. Although not straightforward, a more thorough comparison of strain rates with geologic and seismic observations is recommended for future work. This could potentially, for example, determine whether geodetic, geologic, and seismic moment rates agree in areas that have experienced a major earthquake. Comparing interseismic strain rate orientations and seismic stress orientations could potentially also produce interesting results if done within the context of earthquake cycle modeling.



CONCLUSIONS

We summarize our observations of strain rates in New Zealand as follows:

- 1. One principal result from the different strain rate analyses conducted for this study is that the inferred strain rate field in New Zealand is quite similar across all methods used in this study; spatially averaged maximum shear strain rates from the mean models vary from 0.1 to 0.12 microstrain/yr, disagreeing at about the 20% level, and spatially averaged dilatation rates range between about 0.015 and 0.022 microstrain/yr, disagreeing at the ~40% level. Total variability between methods is on the order of 0.01 microstrain/yr. VDoHS and body force results are relatively smooth due to penalizing strain rate away from observations, whereas VELMAP and geostatistics are comparatively rougher. The Kostrov moment rate computed from all four methods varies from ~ 0.64 to 2.93×10^{19} N·m/yr, with most of the variability in moment rate arising from the choice of seismogenic depth and whether to include offshore strain rates in the calculation.
- Differences in strain rate estimates due to methodology (epistemic uncertainty) can be larger than the formal aleatoric uncertainty from individual methods. This highlights

Figure 16. Inferred strain rate direction and equivalent faulting style for each of the four methods. The Hikurangi signal has been removed from these estimates. (a–d) Strain rate tensors represented as wedge diagrams, in which the width of the wedge represents the 2-sigma uncertainty in direction propagated from the uncertainties in the strain rate components. Red symbols indicate extension, and blue bars/wedges indicate shortening rates. (e–h) Inferred style based on the strain rate tensors. The color version of this figure is available only in the electronic edition.

the need for considering multiple strain rate methods and averaging results, particularly when using strain rates for seismic hazard purposes. The variability among strain-rate methods is a result of how the different methods handle sparse station spacing and variable strain rate gradients. These two spatial variables are interrelated because "sparsity" in station spacing is understood relative to the magnitude of velocity gradients; in areas where velocity gradients are higher than the regional average, the methods tend to differ the most.

 Geodetically estimated strain rates are broadly consistent in style with geologic faulting style, and estimated moment accumulation rates across all methods are within uncertainty of the observed moment from the earthquake catalog. 4. Geodetic data provides valuable insight into seismic hazard that is independent of seismicity and geologic information, and its incorporation with those other sources of information can help better constrain seismic hazard models and/or better canvass the spectrum of defensible epistemic uncertainty. Future work should focus on integrating GNSS with InSAR and systematize the calculation of multiple strain rate methods for a given data set.

DATA AND RESOURCES

The Global Navigation Satellite Systems (GNSS) velocities used in this study are from Beavan et al. (2016). Fault traces and faulting style databases are from the New Zealand Community Fault Model 1.0 (Seebeck et al., 2022, 2023). The supplemental material contains some additional discussion, a table of earthquakes used in the seismic moment calculation, and figures showing data uncertainties, strain rates retaining the Hikurangi subduction signal, and miscellaneous results. Gridded strain rates and MATLAB codes for reproducing the figures in this article are provided through the Open Science Foundation (Maurer et al., 2023). The unpublished manuscript by K. Johnson, L. M. Wallace, J. Maurer, I. Hamling, C. A. Williams, C. Rollins, M. Gerstenberger, and R. Van Dissen, "Inverting geodetic strain rates for slip deficit rate in complex deforming zones: An application to the New Zealand plate boundary," submitted to J. Geophys. Res.

DECLARATION OF COMPETING INTERESTS

The authors declare no competing interests.

ACKNOWLEDGMENTS

The authors thank John Townend, Jessica Murray, and Ned Field for reviewing the original New Zealand National Seismic Hazard Model 2022 (NZ NSHM 2022) report (Johnson et al., 2022) that greatly improved this article. The authors also thank Bill Hammond, an anonymous reviewer, and Guest Editor Jarg Pettinga for providing helpful and encouraging comments, which greatly improved this article. This work was funded by the New Zealand Ministry of Business, Innovation, and Employment for GNS Science via the National Seismic Hazard Model 2022 Revision Project (Contract 2020-BD101).

REFERENCES

- Árnadóttir, T., J. Haines, H. Geirsson, and S. Hreinsdóttir (2018). A preseismic strain anomaly detected before M6 earthquakes in the south Iceland Seismic zone from GPS station velocities, J. Geophys. Res. 123, no. 12, 11,091-11,111, doi: 10.1029/2018JB016068.
- Aster, R. C., B. Borchers, and C. H. Thurber (2018). Parameter Estimation and Inverse Problems, Elsevier, Oxford, United Kingdom.
- Baxter, S. C., S. Kedar, J. W. Parker, F. H. Webb, S. E. Owen, A. Sibthorpe, and D. Dong (2011). Limitations of strain estimation techniques from discrete deformation observations, Geophys. Res. Lett. 38, no. 1, doi: 10.1029/2010GL046028.
- Beavan, J., and J. Haines (2001a). Contemporary horizontal velocity and strain rate fields of the Pacific-Australian plate boundary

- zone through New Zealand, J. Geophys. Res. 106, no. B1, 741-770, doi: 10.1029/2000JB900302.
- Beavan, J., and J. Haines (2001b). Contemporary horizontal velocity and strain rate fields of the Pacific-Australian plate boundary zone through New Zealand, J. Geophys. Res. 106, no. B1, 741, doi: 10.1029/2000JB900302.
- Beavan, J., L. M. Wallace, N. Palmer, P. Denys, S. Ellis, N. Fournier, S. Hreinsdottir, C. Pearson, and M. Denham (2016). New Zealand GPS velocity field: 1995-2013, N. Z. J. Geol. Geophys. 59, no. 1, 5-14, doi: 10.1080/00288306.2015.1112817.
- Bird, P., D. D. Jackson, Y. Y. Kagan, C. Kreemer, and R. S. Stein (2015). GEAR1: A global earthquake activity rate model constructed from geodetic strain rates and smoothed seismicity, Bull. Seismol. Soc. Am. 105, no. 5, 2538-2554, doi: 10.1785/0120150058.
- Cai, J., and E. W. Grafarend (2007). Statistical analysis of geodetic deformation (strain rate) derived from the space geodetic measurements of BIFROST Project in Fennoscandia, J. Geodynam. 43, no. 2, 214-238, doi: 10.1016/j.jog.2006.09.010.
- Chanier, F., J. Ferrière, and J. Angelier (1999). Extensional deformation across an active margin, relations with subsidence, uplift, and rotations: The Hikurangi subduction, New Zealand, Tectonics 18, doi: 10.1029/1999TC900028.
- Dimitrova, L. L., L. M. Wallace, A. J. Haines, and C. A. Williams (2016). High-resolution view of active tectonic deformation along the Hikurangi subduction margin and the Taupo Volcanic Zone, New Zealand, N. Z. J. Geol. Geophys. 59, no. 1, 43-57.
- El-Fiky, G. S., and T. Kato (1999). Interplate coupling in the Tohoku district, Japan, deduced from geodetic data inversion, J. Geophys. Res. 104, no. B9, 20361, doi: 10.1029/1999JB900202.
- England, P., and P. Molnar (1997). The field of crustal velocity in Asia calculated from Quaternary rates of slip on faults, Geophys. J. Int. 130, no. 3, 551-582, doi: 10.1111/j.1365-246X.1997.tb01853.x.
- Engwirda, D. (2014). Locally-optimal Delaunay-refinement and optimisation-based mesh generation, Ph.D. Thesis, School of Mathematics and Statistics, The University of Sydney, available at http://hdl.handle.net/2123/13148 (last accessed November 2023).
- Feigl, K. L., D. C. Agnew, Y. Bock, D. Dong, A. Donnellan, B. H. Hager, T. A. Herring, D. D. Jackson, T. H. Jordan, R. W. King, et al. (1993). Space geodetic measurement of crustal deformation in central and southern California, 1984—1992, J. Geophys. Res. 98, no. B12, 21,677-21,712.
- Field, E. H., R. J. Arrowsmith, G. P. Biasi, P. Bird, T. E. Dawson, K. R. Felzer, D. D. Jackson, K. M. Johnson, T. H. Jordan, C. Madden, et al. (2014). Uniform California earthquake rupture forecast, version 3 (UCERF3): The Time-Independent Model, Bull. Seismol. Soc. Am. 104, no. 3, 1122-1180.
- Franklin, K. R., and M.-H. Huang (2022). Revealing crustal deformation and strain rate in Taiwan using InSAR and GNSS, Geophys. Res. Lett. 49, no. 21, e2022GL101306, doi: 10.1029/2022GL101306.
- GNS Science (2022). Augmented NZ earthquake catalogue used in NZ NSHM 2022 [Dataset], GNS Science, doi: 10.21420/1SJE-E991.
- Goudarzi, M. A., M. Cocard, and R. Santerre (2015). GeoStrain: An open source software for calculating crustal strain rates, Comput. Geosci. 82, 1-12, doi: 10.1016/j.cageo.2015.05.007.
- Hackl, M., R. Malservisi, and S. Wdowinski (2009). Strain rate patterns from dense GPS networks, Nat. Hazards Earth Syst. Sci. 9, no. 4, 1177-1187, doi: 10.5194/nhess-9-1177-2009.

- Haines, A. J., and W. E. Holt (1993). A procedure for obtaining the complete horizontal motions within zones of distributed deformation from the inversion of strain rate data, *J. Geophys. Res.* 98, no. B7, 12,057–12,082, doi: 10.1029/93JB00892.
- Haines, A. J., and L. M. Wallace (2020). New Zealand-wide geodetic strain rates using a physics-based approach, *Geophys. Res. Lett.* 47, no. 1, e2019GL084606, doi: 10.1029/2019GL084606.
- Haines, A. J., L. L. Dimitrova, L. M. Wallace, and C. A. Williams (2015). Enhanced Surface Imaging of Crustal Deformation: Obtaining Tectonic Force Fields Using GPS Data, Springer, Cham, Switzerland.
- Haines, J., L. M. Wallace, and L. Dimitrova (2019). Slow slip event detection in Cascadia using vertical derivatives of horizontal stress rates, *J. Geophys. Res.* 124, no. 5, 5153–5173, doi: 10.1029/2018JB016898.
- Hamling, I. J., G. Kilgour, S. Hreinsdóttir, E. Bertrand, and S. Bannister (2022a). Estimating the distribution of melt beneath the Okataina Caldera, New Zealand: An integrated approach using geodesy, seismology and magnetotellurics, *J. Volcanol. Geotherm. Res.* **426**, 107549. doi: 10.1016/j.jvolgeores.2022.107549.
- Hamling, I. J., T. J. Wright, S. Hreinsdóttir, and L. M. Wallace (2022b).
 A snapshot of New Zealand's dynamic deformation field from envisat InSAR and GNSS observations between 2003 and 2011, Geophys. Res. Lett. 49, no. 2, e2021GL096465, doi: 10.1029/2021GL096465.
- Hamling, I. J., S. Hreinsdóttir, and N. Fournier (2015). The ups and downs of the TVZ: Geodetic observations of deformation around the Taupo Volcanic Zone, New Zealand, J. Geophys. Res. 120, no. 6, 4667–4679.
- Handwerger, A. L., M.-H. Huang, E. J. Fielding, A. M. Booth, and R. Bürgmann (2019). A shift from drought to extreme rainfall drives a stable landslide to catastrophic failure, *Sci. Rep.* 9, no. 1, 1569, doi: 10.1038/s41598-018-38300-0.
- Hearn, E. H., K. Johnson, and W. Thatcher (2010). Space geodetic data improve seismic hazard assessment in California, workshop on incorporating geodetic surface deformation data into UCERF3, Pomona, California, 1–2 April 2010, *Eos Trans. AGU* **91,** no. 38, 336, doi: 10.1029/2010EO380007.
- Huang, M. H., K. U. Lopez, and K. G. Olsen (2022). Icequake-magnitude scaling relationship along a rift within the Ross Ice Shelf, Antarctica, *Geophys. Res. Lett.* 49, e2022GL097961, doi: 10.1029/2022GL097961.
- Hussain, E., T. J. Wright, R. J. Walters, D. P. S. Bekaert, R. Lloyd, and A. Hooper (2018). Constant strain accumulation rate between major earthquakes on the north Anatolian fault, *Nat. Commun.* 9, no. 1, 1392, doi: 10.1038/s41467-018-03739-2.
- Johnson, K. (2023). kajjohns/BforStrain: Second release of BforStrain (v1.1.0), Zenodo, doi: 10.5281/zenodo.8139779.
- Johnson, K. M. (2013). Slip rates and off-fault deformation in southern California inferred from GPS data and models, J. Geophys. Res. 118, no. 10, 5643–5664, doi: 10.1002/jgrb.50365.
- Johnson, K. M, L. M. Wallace, J. Maurer, I. J. Hamling, C. A. Williams, C. Rollins, M. C. Gerstenberger, and R. J. Van Dissen (2022). Geodetic deformation model for the 2022 update of the New Zealand National Seismic Hazard Model, Lower Hutt (NZ), doi: 10.21420/P93X-8293.
- Kato, T., G. S. El-Fiky, E. N. Oware, and S. Miyazaki. (1998). Crustal strains in the Japanese islands as deduced from dense GPS

- array, Geophys. Res. Lett. 25, no. 18, 3445-3448, doi: 10.1029/98GL02693.
- Kostrov, V. V. (1974). Seismic moment and energy of earthquakes, and seismic flow of rock, *Izv. Acad. Sci. USSR Phys. Solid Earth* 1, 23–44.
- Kreemer, C., G. Blewitt, and E. C. Klein (2014). A geodetic plate motion and Global Strain Rate Model. *Geochem. Geophys. Geosys.* 15, no. 10, 3849–3889, doi: 10.1002/2014GC005407
- Kreemer, C., J. Haines, W. E. Holt, G. Blewitt, and D. Lavallee (2000). On the determination of a global strain rate model, *Earth Planets Space* **52**, no. 10, 765–770, doi: 10.1186/BF03352279.
- Kreemer, C., W. C. Hammond, and G. Blewitt (2018). A robust estimation of the 3-D intraplate deformation of the north American plate from GPS, *J. Geophys. Res.* **123**, no. 5, 4388–4412.
- Maurer, J., K. Johnson, and P. Segall (2018). Bounding the moment deficit rate on crustal faults using geodetic data: Application to southern California, *J. Geophys. Res.* **123**, no. 12, 11,048–11,061, doi: 10.1029/2018JB016097.
- Maurer, J., and K. Materna (2023). Quantification of geodetic strain rate uncertainties and implications for seismic hazard estimates, *Geophys. J. Int.* doi: 10.1093/gji/ggad191.
- Maurer, J., K. Johnson, L. Wallace, I. Hamling, C. Williams, C. Rollins, M. Gerstenberger, and R. Van Dissen (2023). New Zealand strain rates, doi: 10.17605/OSF.IO/RGPFE.
- Mazzotti, S., X. le Pichon, P. Henry, and S. Miyazaki (2000). Full interseismic locking of the Nankai and Japan-west Kurile subduction zones: An analysis of uniform elastic strain accumulation in Japan constrained by permanent GPS, *J. Geophys. Res.* **105**, no. B6, 13,159–13,177, doi: 10.1029/2000JB900060.
- McCaffrey, R., M. D. Long, C. Goldfinger, P. C. Zwick, J. L. Nabelek, C. K. Johnson, and C. Smith (2000). Rotation and plate locking at the southern Cascadia subduction zone, *Geophys. Res. Lett.* **27**, no. 19, 3117–3120, doi: 10.1029/2000GL011768.
- Menke, W. (2018). Geophysical Data Analysis: Discrete Inverse Theory, Academic Press, Elsevier, Oxford.
- Noda, A., and M. Matsu'ura (2010). Physics-based GPS data inversion to estimate three-dimensional elastic and inelastic strain fields, *Geophys. J. Int.* **182**, no. 2, 513–530, doi: 10.1111/j.1365-246X.2010.04611.x.
- Petersen, M. D., M. P. Moschetti, P. M. Powers, C. S. Mueller, K. M. Haller, A. D. Frankel, Y. Zeng, S. Rezaeian, S. C. Harmsen, O. Boyd, et al. (2014). Documentation for the 2014 update of the United States national seismic hazard maps, U.S. Geol. Surv. Open-File Rept., doi: 10.3133/ofr20141091.
- Pollitz, F. F., E. L. Evans, E. H. Field, A. E. Hatem, E. H. Hearn, K. Johnson, J. R. Murray, P. M. Powers, Z. Shen, C. Wespestad, et al. (2022). Western U.S. deformation models for the 2023 Update to the U.S. National Seismic Hazard Model, Seismol. Res. Lett. 93, no. 6, 3068–3086, doi: 10.1785/0220220143.
- Rastin, S. J., D. A. Rhoades, C. Rollins, M. C. Gerstenberger, A. Christophersen, and K. K. S. Thingbaijam (2022). Spatial distribution of earthquake occurrence for the New Zealand National Seismic Hazard Model revision, GNS Science Rept. 2021/51, GNS Science, Lower Hutt (NZ), 65 pp., doi: 10.21420/YKQ8-1C41.
- Rastin, S. J., D. A. Rhoades, C. Rollins, M. C. Gerstenberger, A. Christophersen, and K. K. S. Thingbaijam (2023). Spatial distribution of earthquake occurrence for the New Zealand

- National Seismic Hazard Model revision, under review for Bull. Seismol. Soc. Am.
- Reid, H. F. (1910). The California earthquake of April 18, 1906, Report of the State Earthquake Investigation Commission, Vol. 2, 16-18.
- Rhoades, D. A., A. Christophersen, and M. C. Gerstenberger (2017). Multiplicative earthquake likelihood models incorporating strain rates, Geophys. J. Int. 208, no. 3, 1764-1774, doi: 10.1093/gji/ ggw486.
- Sandwell, D. T., and P. Wessel (2016). Interpolation of 2-D vector data using constraints from elasticity, Geophys. Res. Lett. 43, no. 20, 10,703-10,709, doi: 10.1002/2016GL070340.
- Sandwell, D. T., Y. Zeng, Z. K. Shen, B. Crowell, J. Murray, R. McCaffrey, and X. Xu (2016). The SCEC community geodetic model V1: Horizontal velocity grid, Poster 141, SCEC Contribution 6967, SCEC Annual Meeting, Palm Springs, California.
- Savage, J. C. (1983). A dislocation model of strain accumulation and release at a subduction zone. J. Geophys. Res. 88, no. B6, 4984-4996.
- Savage, J. C., and R. W. Simpson (1997). Surface strain accumulation and the seismic moment tensor, Bull. Seismol. Soc. Am. 87, no. 5,
- Savage, J. C., W. Gan, and J. L. Svarc (2001). Strain accumulation and rotation in the eastern California shear zone, J. Geophys. Res. 106, no. B10, 21,995-22,007, doi: 10.1029/2000JB000127.
- Seebeck, H., R. Van Dissen, N. Litchfield, P. Barnes, A. Nicol, R. Langridge, D. Barrell, P. Villamor, S. Ellis, M. Rattenbury, et al. (2022). New Zealand Community Fault Model - version 1.0, GNS Science Rept. 2021/57, GNS Science, Lower Hutt (NZ), 96 pp.
- Seebeck, H., R. Van Dissen, N. Litchfield, P. M. Barnes, A. Nicol, R. Langridge, D. J. A. Barrell, P. Villamor, S. Ellis, M. Rattenbury, et al. (2023). The New Zealand Community Fault Model version 1.0: An improved geological foundation for seismic hazard modelling, N. Z. J. Geol. Geophys. doi: 10.1080/ 00288306.2023.2181362.
- Shen, Z., M. Wang, Y. Zeng, and F. Wang (2015). Optimal interpolation of spatially discretized geodetic data, Bull. Seismol. Soc. Am. 105, no. 4, 2117-2127, doi: 10.1785/0120140247.
- Shen, Z.-K., D. D. Jackson, and B. X. Ge (1996). Crustal deformation across and beyond the Los Angeles basin from geodetic measurements, J. Geophys. Res. 101, no. B12, 27,957-27,980, doi: 10.1029/ 96JB02544.
- Song, X., Y. Jiang, X. Shan, W. Gong, and C. Qu (2019). A fine velocity and strain rate field of present-day crustal motion of the northeastern Tibetan plateau inverted jointly by InSAR and GPS, Remote Sensing 11, no. 4, 10.3390/rs11040435.
- Stevens, V. L., and J.-P. Avouac (2021). On the relationship between strain rate and seismicity in the India-Asia collision zone: Implications for probabilistic seismic hazard, Geophys. J. Int. 226, no. 1, 220-245, doi: 10.1093/gji/ggab098.

- Tape, C., P. Musé, M. Simons, D. Dong, and F. Webb (2009). Multiscale estimation of GPS velocity fields, Geophys. J. Int. 179, no. 2, 945-971, doi: 10.1111/j.1365-246X.2009.04337.x.
- Tarayoun, A., S. Mazzotti, M. Craymer, and J. Henton (2018). Structural inheritance control on intraplate present-day deformation: GPS strain rate variations in the Saint Lawrence Valley, eastern Canada, J. Geophys. Res. 123, no. 8, 7004-7020, doi: 10.1029/2017JB015417.
- Tymofyeyeva, E., and Y. Fialko (2018). Geodetic evidence for a blind fault segment at the southern end of the San Jacinto fault zone, J. Geophys. Res. 123, no. 1, 878-891, doi: 10.1002/2017JB014477.
- Wallace, L. M., J. Beavan, S. Bannister, and C. A. Williams (2012). Simultaneous long-term and short-term slow slip events at the Hikurangi subduction margin, New Zealand: Implications for processes that control slow slip event occurrence, duration, and migration, J. Geophys. Res. 117, no. B11, 10.1029/2012JB009489.
- Wallace, L. M., J. Beavan, R. McCaffrey, K. Berryman, and P. Denys (2007). Balancing the plate motion budget in the South Island, New Zealand using GPS, geological and seismological data, Geophys. J. Int. 168, no. 1, 332-352, doi: 10.1111/j.1365-246X.2006.03183.x.
- Wallace, L. M., J. Beavan, R. McCaffrey, and D. Darby (2004). Subduction zone coupling and tectonic block rotations in the North Island, New Zealand, J. Geophys. Res. 109, no. B12, doi: 10.1029/2004JB003241.
- Wang, H., and T. J. Wright (2012). Satellite geodetic imaging reveals internal deformation of western Tibet, Geophys. Res. Lett. 39, no. 7, 10.1029/2012GL051222.
- Wang, H., T. J. Wright, J. Liu-Zeng, and L. Peng (2019). Strain rate distribution in south-central Tibet from two decades of InSAR and GPS, Geophys. Res. Lett. 46, no. 10, 5170-5179, doi: 10.1029/ 2019GL081916.
- Weiss, J. R., R. J. Walters, Y. Morishita, T. J. Wright, M. Lazecky, H. Wang, E. Hussain, A. J. Hooper, J. R. Elliott, C. Rollins, et al. (2020). High-resolution surface velocities and strain for Anatolia from Sentinel-1 InSAR and GNSS data, Geophys. Res. Lett. 47, no. 17, e2020GL087376, doi: 10.1029/2020GL087376.
- Wu, Y., Z. Jiang, G. Yang, W. Wei, and W. Liu (2011). Comparison of GPS strain rate computing methods and their reliability, Geophys. *J. Int.* **185,** no. 2, 703–717, doi: 10.1111/j.1365-246X.2011.04976.x.
- Xu, X., D. T. Sandwell, E. Klein, and Y. Bock (2021). Integrated Sentinel-1 InSAR and GNSS time-series along the San Andreas fault system, J. Geophys. Res. 126, no. 11, e2021JB022579, doi: 10.1029/2021JB022579.
- Zeng, Y., M. D. Petersen, and Z.-K. Shen (2018). Earthquake potential in California-Nevada implied by correlation of strain rate and seismicity, Geophys. Res. Lett. 45, no. 4, 1778-1785, doi: 10.1002/ 2017GL075967.

Manuscript received 21 June 2023 Published online 22 November 2023